REPORT DOCUMENTATION PAGE

AFRL-SR-AR-TR-03-

0479

1. REPORT DATE (DD-MM-YYYY)	2. REPORT TYPE	3. DATES COVERED (From - To)
	Final Technical	01-06-1998 - 31-05-2002

4. TITLE AND SUBTITLE

(U) Mixing and Combustion in Vortex Dominated Combustors with Distributed Air- and Fuel-Injection

5a. CONTRACT NUMBER

5b. GRANT NUMBER
F49620-98-1-0476

5c. PROGRAM ELEMENT NUMBER
61103D

6. AUTHOR(S)

Sumanta Acharya, Professor, Mechanical Engineering Department, Louisiana State University
Michael Murphy, Associate Professor, Mechanical Engineering Department, Louisiana State University

5d. PROJECT NUMBER
3484

5e. TASK NUMBER
BS

5f. WORK UNIT NUMBER

7. PERFORMING ORGANIZATION NAME(S) AND ADDRESS(ES)

Louisiana State University
Baton Rouge LA 70803

8. PERFORMING ORGANIZATION REPORT NUMBER

9. SPONSORING / MONITORING AGENCY NAME(S) AND ADDRESS(ES)

AFOSR/NA
4015 Wilson Boulevard
Room 713
Arlington VA 22203-1954

11. SPONSOR/MONITOR'S REPORT NUMBER(S)

12. DISTRIBUTION / AVAILABILITY STATEMENT

Approved for public release; distribution is unlimited

13. SUPPLEMENTARY NOTES

14. ABSTRACT

Measurements of temperature, velocity and emissions were performed in two trapped vortex combustor configurations, and several strategies for improving key performance metrics (e.g., circumferential uniformity in temperature and NOx emissions) were examined. The measurements show that introducing swirl with the primary cavity air reduces NOx emissions, extends the Lean Blow Out (LBO) limit and decreases circumferential non-uniformity in the temperature. With the inner-cavity configuration, LBO values as low as 0. 1 and single-digit NOx were achieved. With the outer-cavity configuration, LBO occurred at 0.3. Computations performed indicate that the cavity vortex has a toroidal donut shape, and has large scale dynamics. Distributed micro-scale fuel injectors were fabricated as part of this effort, and have the potential for generating an uniform dispersion of small droplets desirable for improved combustion characteristics. Temperature-actuated bi-morph valves were also developed for control of dilution air and local stoichiometry.

15. SUBJECT TERMS

Trapped Vortex Combustion, Micro-fuel-injectors, Dilution-jet Control

16. SECURITY CLASSIFICATION OF:			17. LIMITATION OF ABSTRACT	18. NUMBER OF PAGES	19a. NAME OF RESPONSIBLE PERSON
a. REPORT	b. ABSTRACT	c. THIS PAGE			Julian M. Tishkoff
nclassified	Unclassified	Unclassified	UL	49	19b. TELEPHONE NUMBER (include area code) (703) 696-8478

PERFORMANCE REPORT
GRANT NUMBER: F49620-98-1-0476

Objectives

The specific goals of the present research are:

1. To provide a fundamental understanding of the flow and transport mechanisms in the Trapped Vortex (TV) combustor through detailed measurements and numerical studies.
2. To examine improved TV combustor configurations. Improvement strategies examined include: introduction of swirl in the cavity and alternate injection configurations.
3. To develop micro- fuel injector arrays and temperature-actuated bi-morph actuators for mixing enhancement and control.

Status of the Effort

The three major goals of the effort, as noted above, were achieved. Improved fundamental understanding was addressed through measurements of temperature, velocity and emissions, and computations in two trapped vortex combustor configurations (termed inner- and outer cavity). Several strategies for improving key performance metrics (e.g., circumferential uniformity in temperature and NOx emissions) were examined. Introducing swirl with the primary cavity air was shown to reduce NOx emissions, extend the Lean Blow Out (LBO) limit and decrease circumferential non-uniformity in the temperature. With the inner-cavity configuration, LBO values as low as 0. 1 and single-digit NOx were achieved. With the outer-cavity configuration, LBO occurred at 0.3. Computations performed indicate that the cavity vortex has a toroidal donut shape, and has large scale dynamics. Distributed micro-scale fuel injectors were fabricated as part of this effort, and have the potential for generating an uniform dispersion of small droplets desirable for improved combustion characteristics. Temperature-actuated bi-morph valves were also developed for control of dilution air and local stoichiometry. Additional work is needed to demonstrate combustion improvements using micro-fuel-injector arrays, and bi-morph dilution-jet valves.

Accomplishments/New Findings

Key accomplishments include:

- Swirl-induced reduction of temperature non-uniformity, emissions, and extension of LBO
- Detailed measurements and computations in the inner-cavity and outer-cavity configurations leading to an improved understanding of the flow and combustion behavior
- Evaluation of alternate cavity-injection strategies for improved performance metrics (heat release, circumferential-temperature uniformity, and emissions)
- Development and fabrication of micro-scale-fuel-injector arrays (metal and ceramic)
- Development and fabrication of temperature-actuated bi-morph valves/actuators for dilution-jet control

Personnel Supported

Faculty: Professor Sumanta Acharya, Professor Mike Murphy
Post-Doc: Dr. P. Chakka

Graduate Students: Mayank Tyagi, Tracy Morris, Proyag Dutta, Guoqiang Li, Paulo Caesar Mancilla

Publications

1. Chakka, P., Mancilla, C., and Acharya, S., "Flame Stability in a Trapped Vortex Combustor" APS Meeting, New Orleans, Nov. 1999, *Bulletin of the American Physical Society, Vol. 44, No. 8, p. 91*

2. Mancilla, C., Chakka, P., and Acharya, S., Performance of a Trapped Vortex Spray Combustor, *ASME-Intl. Gas Turbine Conference*, June 2001, New Orleans

3. Acharya, S., and Mancilla, C., Measurements and Simulations in a Trapped Vortex Combustor Configuration: Performance Characterization, To be Submitted (*Combustion Science and Technology*)

4. Acharya, S., and Mancilla, C., Improvements in Circumferential Mixing Through Swirl Injection in a Trapped Vortex Combustor Configuration, To be Submitted *(AIAA Journal of Power and Propulsion*)

5. Tyagi, M., and Acharya, S., Large Eddy Simulations of Complex Turbulent Flows Using Immersed Boundary Methods, *Third AFOSR International Conference on Direct Numerical Simulation and Large Eddy Simulation*, Arlington, August 2001

6. Tyagi, M., and Acharya, S., Large Eddy Simulations in a Trapped Vortex Combustor Configuration, To be Submitted (*Computers and Fluids*)

7. Tyagi, M., and Acharya, S., Larged Eddy Simulations in Complex Geometries Using the Immersed Boundary Technique, *ASME International Mechanical Engineering Congress and Expo,* Wasshington D.C., Nov. 2003, accepted

8. Acharya, S., and Chakka, P., Flame Stabilization in a Can Combustor through an External Trapped Vortex Cavity, P. Chakka and S. Acharya, To be Submitted *(AIAA Journal of Power and Propulsion*)

9. Palaparti, D., Landin, S., Simmons, H., Ritland, M., Sommerfeldt, R., Desta, Y.M., Morris, T.E., and Murphy, M.C., Injection molded ceramic micro-components," at *HARMST 2003,* Monterey, CA, June 15-17,2003.

10. Datta, P., Sathe, M., Namburi, L., Podlaha, E.J., Acharya, S. and Murphy, M.C., Microfabricated bimetallic actuator, in *MEMS Components and Applications for Industry, Automobiles, Aerospace, and Communication II,* ed. S.W. Janson, Society of Photo-optical Instrumentation Engineers (SPIE), Volume 4981, 2003, pp. 83-94.

11. Morris, T.E., Murphy, M.C., and Acharya, S., Microfabrication of a metal fuel injector nozzle array," in *Micromachining and Microfabrication Process Technology"* IV, eds.

J.M. Karam and J. Yasaitis, Society of Photo-optical Instrumentation Engineers (SPIE), Volume 4174, 2000, pp. 58-65.

12. Datta, P., Namburi, L., Podlaha, E.J., Acharya, S., and Murphy, M.C., Design and Fabrication of Thermomechanical Microactuator for High Temperature Applications," at *HARMST 2001*, Baden-Baden, Germany, June 2001

13. Datta, P., Sathe, M., Namburi, L., Podlaha, E.J., Acharya, S. and Murphy, M.C., "Microfabricated bimetallic actuator," in *MEMS Components and Applications for Industry, Automobiles, Aerospace, and Communication II,* ed. S.W. Janson, Society of Photo-optical Instrumentation Engineers (SPIE), Volume 4981, pp. 83-94, 2003

Interactions/Transitions

a. Meetings, Conferences: See above

Inventions/Patents

Patent application filed with the university: Electrodeposition of Invar for Bi-morph actuator, Mike Murphy et al.

FINAL DETAILED REPORT

For Project Entitled

MIXING AND COMBUSTION IN VORTEX DOMINATED COMBUSTORS WITH DISTRIBUTED AIR- AND FUEL- INJECTION

AFOSR GRANT NUMBER F49620-98-1-0476

Contract Monitor

Dr. Julian Tishkoff
Manager, Propulsion Program
AFOSR

Principal Investigator(s)

Professor Sumanta Acharya
Ph: 225-388-5809 email: acharya@me.LSU.edu
Professor Michael Murphy

Mechanical Engineering Department
Louisiana State University
Baton Rouge, LA 70803

Submitted Through

Board of Regents
150 Third Street, Suite 129
Baton Rouge, LA 70801

I. ABSTRACT

Flame instability in gas turbine combustors is a major source for reduced fuel efficiency and blowout. The present research deals with an improved concept of flame stabilization where a vortex, trapped in a cavity, is used to stabilize the flame. Two combustor configurations embodying this improved concept (called Trapped Vortex Combustors) have been examined in the present work. In the first configuration, the Trapped Vortex (TV) combustor is a circumferential cavity formed between a forebody and an afterbody. Fuel and air are directly injected into the cavity to sustain a flame. In the second configuration, the TV is formed in an annular cavity mounted along the periphery of the main combustor. Hot combustion products emanating from within the cavity get entrained into the main combustion zone thus providing ignition of the primary fuel/air mixture and the necessary flame stabilization mechanism.

The first major objective of the work was to investigate the flow and combustion behavior in a trapped vortex combustor configuration, and to gain an understanding of the basic mechanisms to guide further development. The second major objective of the work was to explore the development of (1) distributed micro-fuel-injector arrays for generating smaller, more uniformly distributed array of droplets, and (2) distributed micro-actuators for controlling the local stochiometry through air-injection from distributed ports located along the combustor walls.

The performance of both trapped vortex combustors have been investigated experimentally and numerically in the present work. Measurements made include: exhaust emissions (NOx, CO, CO_2, UHC), temperature and velocity distributions inside the cavity, pressure fluctuations, and IR signatures. Computations include the solution of the Reynolds-Averaged-Navier Stokes equations with a k-ε turbulence model and a PDF combustion chemistry model. Large Eddy Simulations of the non-reacting flow have also been performed to understand the fluid dynamical interaction between the cavity flow and the annular flow.

The major achievements of the work have been the following: (1) establishment of stable flames at overall equivalence ratios as low as 0.08 in a liquid-fueled TV combustor; (2) improvements in the circumferential mixing in the cavity, and enhancement in the mixing between the cavity and the annular flow, through the introduction of swirl in the cavity; (3) improved understanding of the fluid dynamical interactions of the cavity flow with the annular flow through Large Eddy Simulations; (4) development and fabrication of MEMS based fuel injectors for distributed injection and improved fuel-air mixing; and (5) design and fabrication of passively and actively controlled valves for local control of dilution airflow.

II. INTRODUCTION

Flame stability is one of the most important issues in the design of gas turbine combustors. Traditionally, swirl or bluff-bodies have been used for flame stabilization. In both cases, a central-recirculation region is formed which transports hot combustion gases to the injection plane, and provides the mechanism for flame stability. However, under lean conditions, flame instabilities and blowout are observed, leading to degradation in the combustor performance.

The concept of cavity based flame holders has also been investigated for both low speed and high speed reacting flow applications. Roudakov et al. (1993), Ben-Yakar and Gany (1994, 1998), Segal et al. (1997), Tishkoff et al. (1997), Baurle and Gruber (1998), and Mathur et al. (1999), have presented the application of cavity based flame holders for supersonic flow

combustors. More recently, Hsu et al. (1995) have proposed a Trapped-Vortex (TV) combustor where flame stability is enhanced due to a stable vortex trapped inside the cavity. Their design consists of a concentric forebody and afterbody with fuel injected from the afterbody. They achieved peak combustion efficiencies in the range 96.7 to 99% with this configuration and very low overall lean-blow-out (LBO) equivalence ratios. The choice of geometrical parameters was based on the aerodynamic studies of Mair (1965) and Little and Whipkey (1979) who found that a stable vortex was formed when the drag was a minimum. Through PIV (Particle Image Velocimetry) measurements, Hsu et al. (1995) have shown that the lowest pressure drop and a stable vortex was obtained when the length of the cavity is 0.59 times the forebody diameter. Katta and Roquemore (1996,1998) performed numerical simulations and demonstrated (consistent with Little and Whipkey's results) that a stable vortex would be trapped in the cavity when the stagnation point was located at the downstream corner of the cavity. By analyzing the lean-blow-out data, Sturgess and Hsu (1997) found that the entrainment of the main annular flow into the cavity is minimal when a vortex is trapped inside the cavity.

III. GOALS OF THE WORK

The specific goals of the present research are:

4. To provide a fundamental understanding of the flow and transport mechanisms in the TV combustor through detailed measurements and numerical studies.
5. To examine improved TV combustor configurations. Improvements can be achieved through greater circumferential mixing of fuel and air in the TV cavity and control of local stoichiometry and air-fuel distributions.
6. To develop MEMS based fuel injectors and actuators for mixing enhancement and control.

The report below will provide a brief description of (1) the experimental facilities, (2) measurements and computations done in support of the first two goals, and (3) design, development and fabrication of the MEMS fuel-injectors and actuators.

IV. EXPERIMENTAL SETUP

Three different TV configurations have been designed and built. The first configuration (inner TV) corresponds to the TV combustor configuration of Hsu et al. (1995) adapted for liquid fuel injection. In the second configuration (outer TV) an annular TV cavity is mounted along the periphery of a can combustor. The third configurations represents the sector of an annular combustor rig. The primary testing has been performed for the first two configurations.

A. Inner TV Configuration

Figure 1 gives the schematic of the experimental setup used for the inner TV configuration. It is designed based on the experimental configuration of Hsu et al. (1995) and has been adapted for liquid spray combustion in the present study. The cavity is formed between a concentric forebody and an afterbody connected through a stainless steel threaded rod. The afterbody consists of three stainless steel disks sandwiched on top of one another. The two reservoirs formed between these disks are used for fuel and air supply into the cavity. Cavity air (called the primary air in the report) is injected through twelve circumferential holes located along the bottom face of the afterbody (Fig. 2). Fuel is injected through four pressure-atomizing

nozzles from the afterbody. Ceramic insulation is used to cover all the surfaces that are directly exposed to the flame. This is done to prevent vaporization of fuel in the feed lines and to avoid degradation in fuel atomization.

Experiments were conducted with an annular air supply rate of up to 100 scfm and a primary air flow rate of up to 30 scfm. Both the primary air stream and the secondary air stream are supplied to the combustion chamber at an ambient temperature of 298 ^{0}K.

Ethanol is used as the liquid fuel. The fuel tank is pressurized up to 120 psig which yields a flow rate of 0.5 gph through each of the four nozzles in the TV combustor. The combustor shell is equipped with optical access for LDV velocity measurements and for Infrared imaging. The inner diameter of the 24-inch long combustor shell is 5.5-inches. High sensitivity, water-cooled pressure transducers (Kistler pressure transducer, Model 7061B0) and heat flux sensors (Vatell Model HFM-6D/H) are mounted along the length of the combustor to measure the pressure and heat flux signatures in the combustor. CO, CO_2, and NO_x emissions and stack temperature are measured using an Enerac Model 3000 integrated emission system. Sapphire windows (1.25" wide and 3.8" long) provide optical access for IR imaging with minimum attenuation in the 3-5 micron infrared spectral band.

An infrared camera (Raytheon Radiance HS) is used to measure the infrared radiation emitted by the flame. The 12-bit Radiance HS camera has a maximum spatial resolution of 256x256 pixels, while the temporal resolution of the camera is inversely proportional to the selected number of pixels per frame. In this study, a 128x128-windowing mode is used with a corresponding 540 Hz maximum frame rate. A two-point normalization of the camera's InSb focal plane array (FPA) is performed using a controlled high temperature oven. This is necessary to prevent sensor saturation and to adjust the gain and offset applied by the camera's processor to enable maximum resolution within the expected levels of incident infrared radiation. The integration time of the camera is set to 2 microseconds to reduce the amount of radiation exposed to the sensor and to maximize the spatial and temporal response of the camera. A hyper-spectral lens (Pacific Advanced Technology) with a 3 to 5 micron spectral bandpass and a 0.01 micron spectral resolution is used to selectively view the CO_2 emission wavelength of approximately 4.3 microns. The images are acquired using a 16-bit 132 megabytes per second framegrabber card (Bitflow Roadrunner Model 12) and processed using Raytheon's ImageDesk II software.

B. Outer TV Configuration

Figure 3 shows the schematic of the outer Trapped Vortex combustor configuration. It consists of three shells of different sizes that are stacked on top of each other. The TV is formed in an annular cavity between the second and third shell. The configuration represents an annular cavity mounted along the periphery of a can combustor. A bluff body is used to stabilize the primary flame in the can combustor. It is expected that the TV flame in the annular cavity will extend the lean flammability range of the primary flame.

The combustor shells are chosen to have a hexagonal cross-section (Figure 3b) in order to have flat optical surfaces for non-invasive measurements. Three adjacent faces of the shell have quartz windows for laser access. Also shown in figure 3b is the flange that acts as an afterbody for the cavity and four injector holders for the injection of fuel into the cavity.

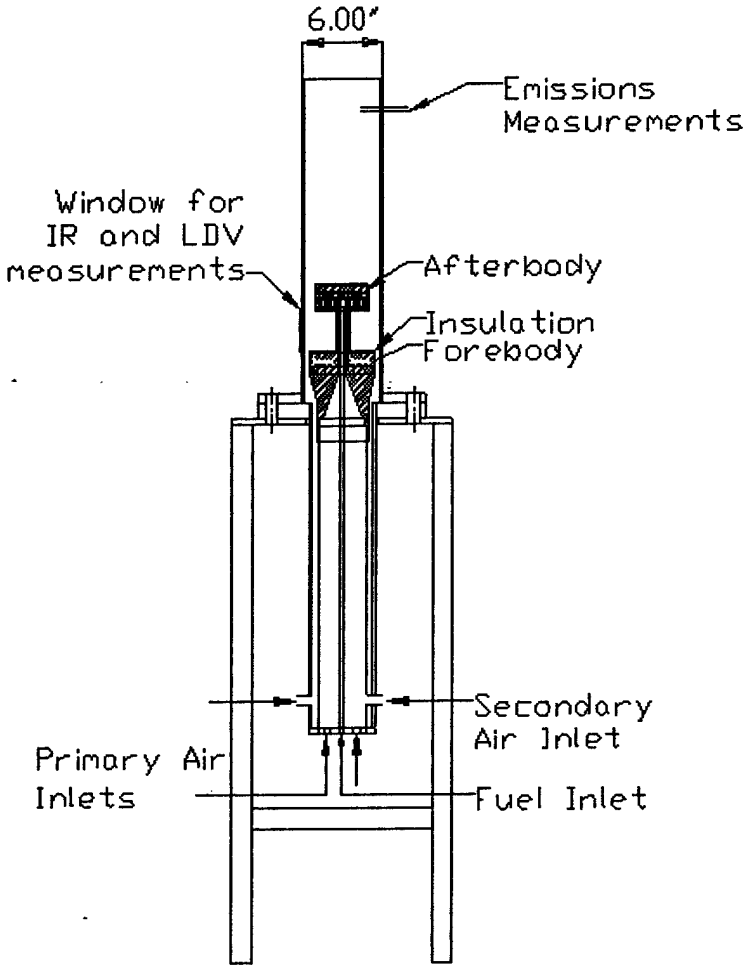

Figure1 Inner TV Combustor Schematic

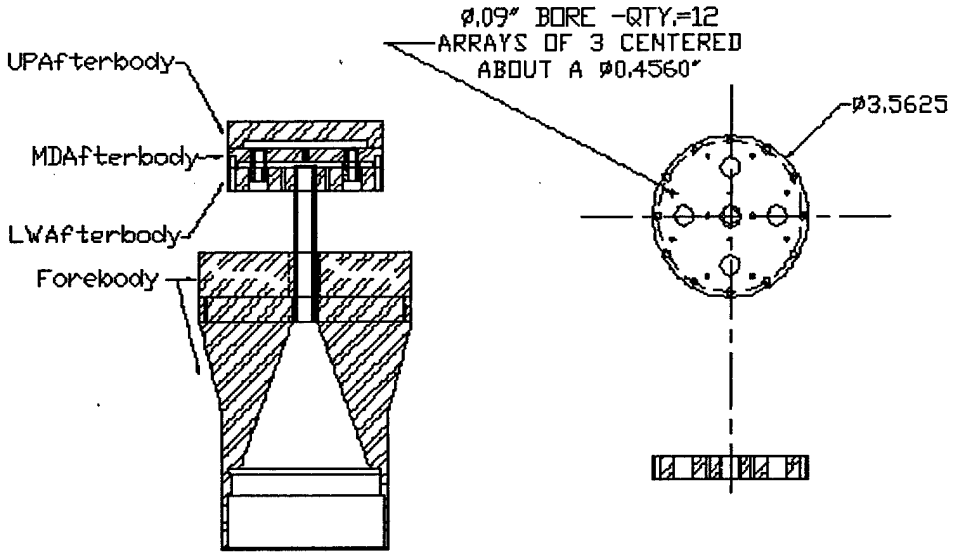

Figure 2 Trapped Vortex Cavity (Nozzle)

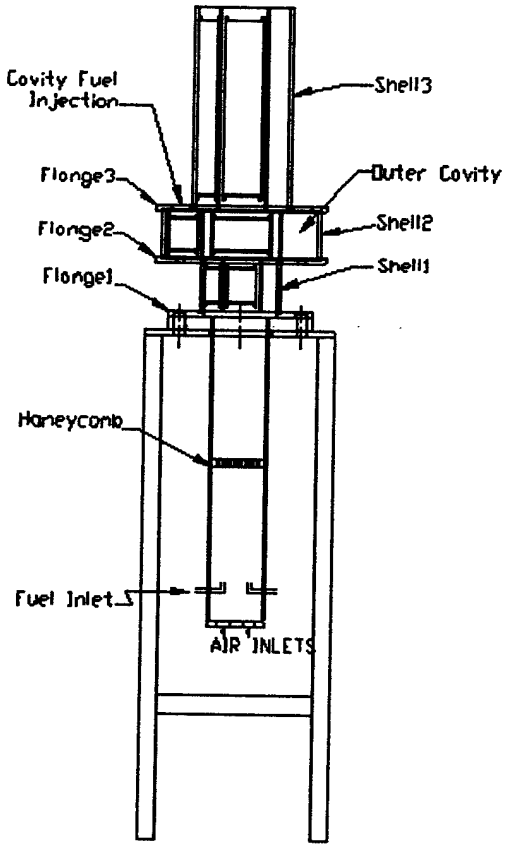

(a)

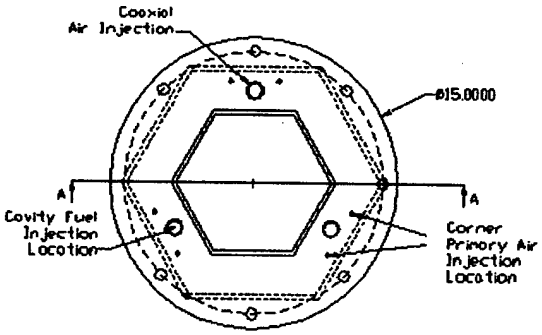

(b)

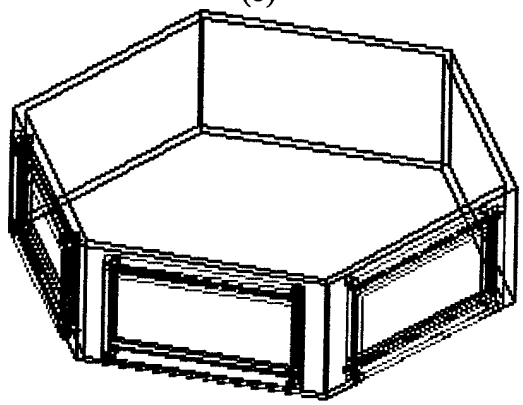

(c)

Figure 3: (a) Schematic of the Outer TV, (b) Details of the Fuel-Injector Locations and (c) Cavity Shell

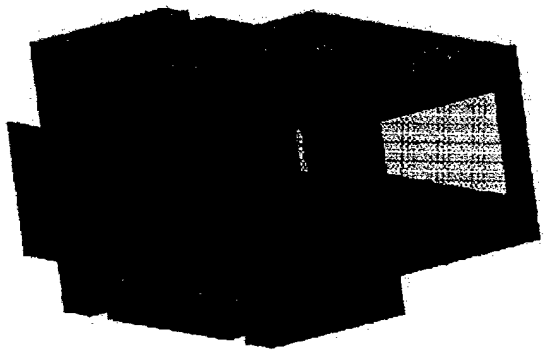

(a)

(b)

Figure 4: (a) Schematic of the Annular TV and (b) Picture of the Annular TV

Primary air into the combustion chamber is supplied from the bottom of the main supply plenum chamber. Liquid/gaseous fuel is injected through four supply tubes located on the side walls of main supply chamber (Figure 3). The supply air is preheated so that the liquid spray is evaporated before reaching the bluff body. Ethanol is used for liquid spray combustion experiments and propane is used for gaseous combustion.

C. Annular TV Configuration

The annular TV configuration is shown in Figure 4, and represents a sector of an annular combustor. The facility was designed and built to operate at a mean operational pressure of about 10 atmospheres. Both the cavity section and the main combustor sections are fitted with quartz windows for optical access.

V. TRAPPED-VORTEX COMBUSTOR: MEASUREMENTS AND COMPUTATIONS

A. Inner TV Configuration

Experiments are performed with liquid fuel for the inner TV configuration. Of specific interest are the flame holding capability and the Lean Blow Out (LBO) limit. The potential of introducing swirl into the cavity for enhanced mixing is also explored, and the results are encouraging. Stable flames can be obtained for equivalence ratios as low as 0.08 with swirl injection.

Measured Temperature Distribution

Temperature distribution inside the cavity is measured with a B-type thermocouple connected to an A/D board. Contour plots of the temperature distribution are presented in Fig. 5 for two azimuthal locations. These measurements are made for a primary equivalence ratio of 0.88 (based on primary air injected into the cavity) and an overall equivalence ratio of 0.12 (based on total air). Figure 5a shows the temperature distribution along an azimuthal plane directly below the fuel injector while Fig. 5b shows the temperature distribution along an azimuthal plane mid-way between the fuel injectors. Peak temperatures in the range of 1200-1300 ^{0}C are seen in the lower half of the cavity. The low temperature region below the fuel spray corresponds to coaxial primary air injected around the fuel injector. However, the presence of low temperature regions near the afterbody in the azimuthal plane mid-way between the fuel injectors indicates poor circumferential mixing. Low temperature regions are also noted in the annular air stream due to insufficient mixing of the cavity flow with the annular flow.

To increase circumferential mixing between the fuel and the air inside the cavity, swirl is introduced into the cavity flow by injecting the air at 30-degree angle from the afterbody. The temperature distributions with swirl air are also shown in Figs 5a and 5b (figure on the right). Higher temperatures and more uniform distributions are obtained with swirl. In the azimuthal plane mid-way between the fuel-injectors, the temperature in most of the cavity is in excess of 1000^{0}C, and in regions close to the afterbody temperatures are higher by 300-400^{0}C relative to the straight injection (no-swirl) case. Furthermore, the temperature distributions are more uniform. In the azimuthal plane containing the fuel injectors, lower temperatures are still observed below the injection location, but the temperature levels are generally higher than those for straight injection. The most significant improvement is seen in the temperatures in the annular flow regions. Higher temperatures, with more uniform temperature distributions are

noted in the annular flow regions, indicating good mixing and entrainment between the cavity flow and the annular flow.

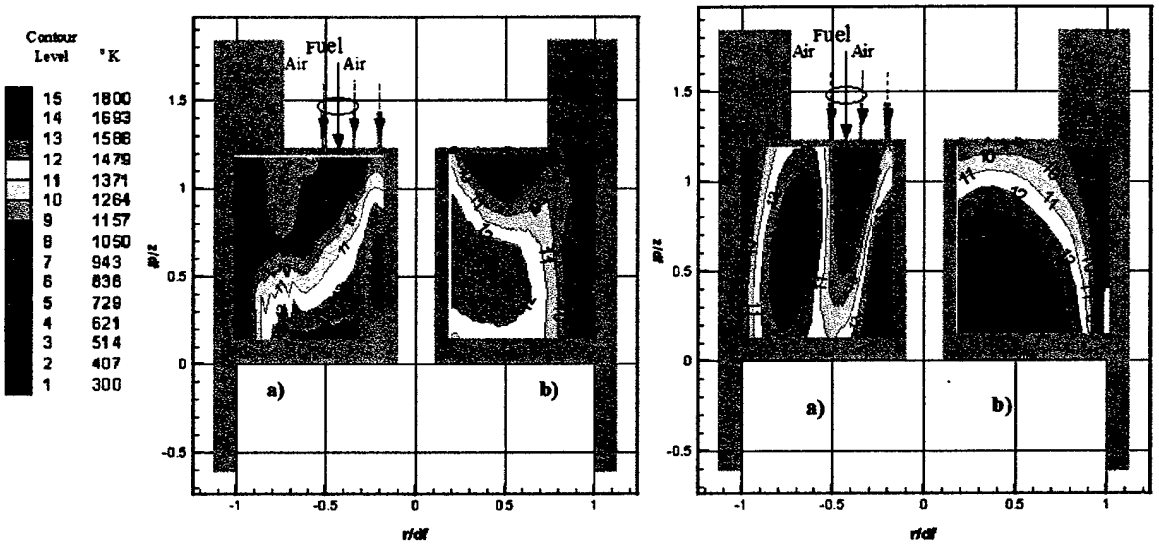

Figure 5: Temperature distribution inside cavity: straight injection-left and swirl injection-right in an azimuthal plane. (a) fuel spray injection plane and (b) injection plane between spray injector locations (Uncertainty=±7 °K)

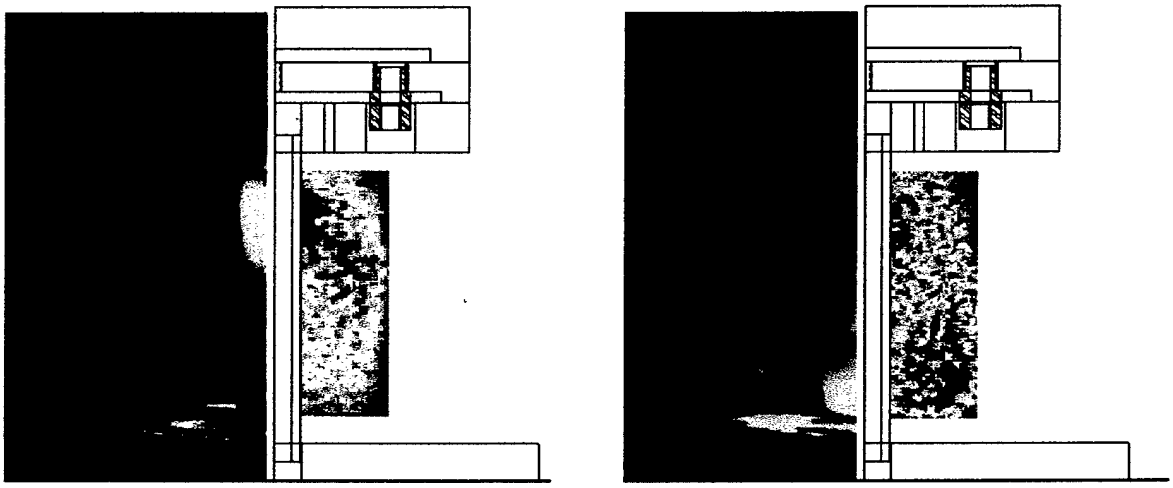

Figure 6: Infrared Plots and CCD images for Φ_p = (a) 3.1 and (b) 1.1 (Annular air velocity = 20 m/s)

Infrared Measurements and CCD Images

Flame characteristics are captured through a quartz shell using a CCD camera. Figure 6 shows two different pictures taken at primary equivalence ratio ϕ_p of 3.14 and 1.1. The difference in the two cases is the velocity of the primary air (and therefore the primary equivalence ratio ϕ_p) injected through the afterbody. For ϕ_p of 3.14, the flame extends outside the cavity, and the highest temperatures are obtained in the vicinity of the afterbody. In Figure

6(a) the greatest pixel intensity in the IR images (right half of the figures) appears near the face of the afterbody. As the primary air is increased, the high temperature regions move closer to the forebody, as indicated by the high-intensity regions in Figure 6(b), and also confirmed by the temperature contours in Fig. 5(a). Based upon both the CCD and IR images, it can be concluded that the velocity of the coaxial injection controls the spreading of the spray and the location of the high-temperature regions where combustion is more intense.

Measured Emissions

Figure 7 shows the Lean Blow Out (LBO) limit for straight and swirl injection. For both cases, the primary air flow rate at LBO decreases as the annular air rate increases, implying that the air entrained into the cavity increases with annular air flow rate. However, at higher annular air flow rates (larger than about 2831 l/min; $\phi_{overall}$>0.175) no additional air is entrained into the trapped vortex. Under these conditions, LBO is determined solely by the characteristics of the fuel and primary air injection. Swirl injection tends to increase the LBO limit. With swirl, there is a slightly greater potential for the annular air to be entrained into the cavity. As the annular air rate is increased, this effect becomes more noticeable. In general, only a small fraction of the main air actually participates in the combustion process at LBO conditions.

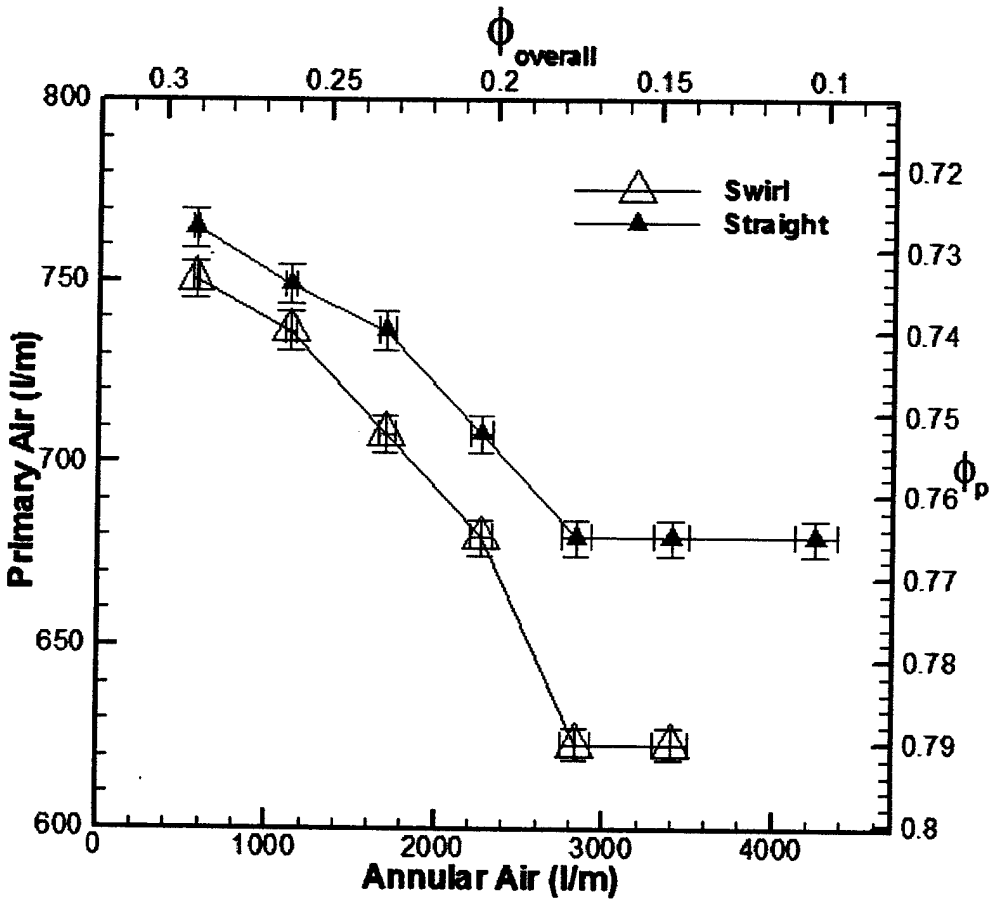

Figure 7: LBO limit for straight and swirl injection

The overall LBO limits (see the top horizontal scale in Fig. 7) obtained (total annular and primary air) for the TV combustor were much lower than those obtained with a conventional can combustor. Overall LBO limits lower than 0.15 were obtained for both vertical and swirl injection, confirming the improved stability of the trapped vortex approach for liquid fuel injection.

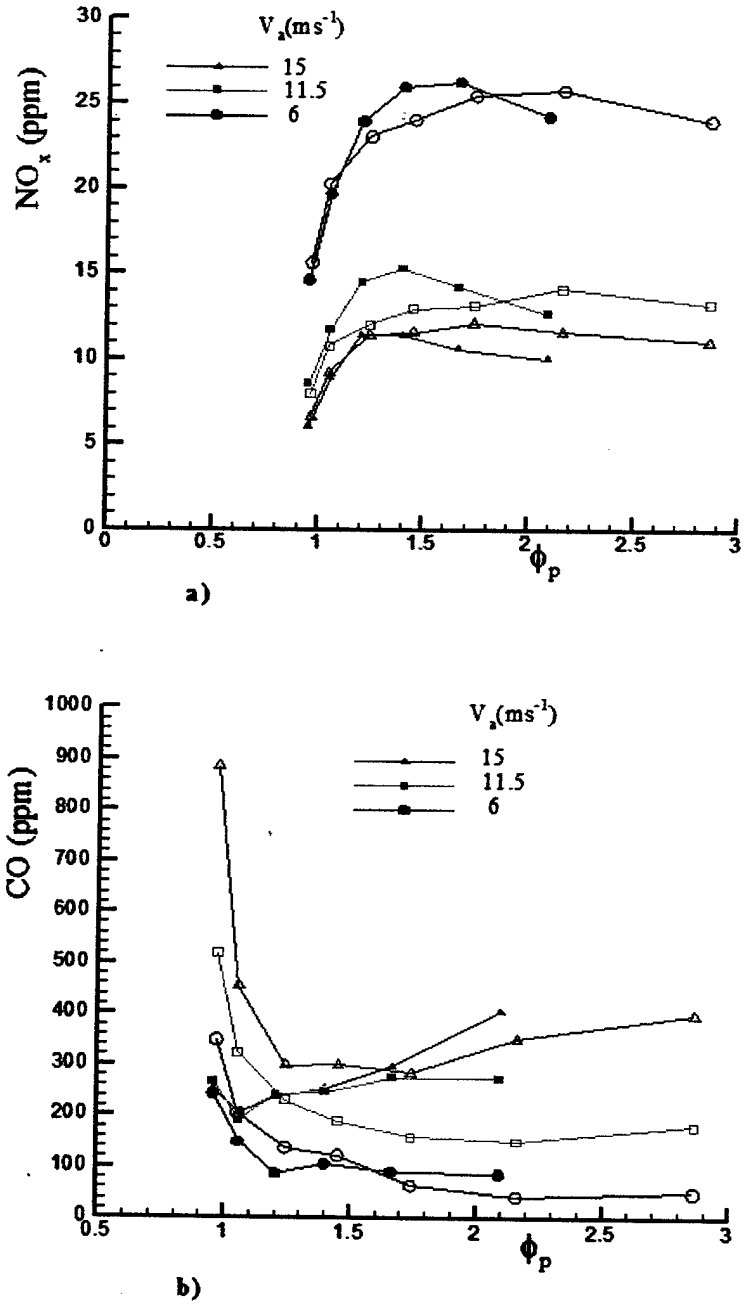

Figure 8: (a) NO_X and (b) CO emissions with angular air injection (open symbols) and straight injection (filled symbols)

The NOx emissions shown in Fig. 8 (a) show that the peak values for the straight injection case occur in the ϕ_p range of 1.25-1.7, depending on the annular air velocity. For this equivalence ratio range, temperatures are highest in the cavity. As the equivalence ratio is lowered and overall equivalence ratios approach fuel lean conditions, the temperature levels drop, and there is a rapid decay in the NOx values. For ϕ_p <1.25, the primary air flow rates are large, resulting in lower residence times of the fuel in the cavity. Both the low temperature and reduced residence time of the reacting fuel in the primary zone are responsible for the decrease in NOx when ϕ_p<1.25. Due to the lower temperatures for ϕ_p<1.25, the combustion process is not complete and results in high CO values.

For swirl injection, the NOx values are generally lower and reach their peak values (with CO reaching corresponding minimum levels) for ϕ_p in the range of 1.5-2. This is a consequence of improved circumferential mixing and uniform temperatures with swirl injection. For ϕ_p>1.5, the NOx and CO levels remain fairly constant, indicating that the mixing process in the cavity is strong enough to efficiently mix the additional fuel injected. **These observations are encouraging and indicate that TV combustors should be designed with swirl.**

Reynolds-Averaged Navier Stokes Simulations (RANS) for the Inner TV

The turbulent-flow equations were solved using a two-equation model for turbulence. The dispersed phase (droplets) were solved in a Lagrangian framework. The coupling between the phases are included in the calculation. Models for droplet heat up, turbulent eddy-droplet interaction, and droplet vaporization are included. Turbulence-chemistry closure is performed with the mixture fraction/PDF approach, which involves the solution of transport equations for two conserved scalars. Physical properties of chemical species and equilibrium data are obtained from the chemical database corresponding to ethanol (C_2H_5OH) and air.

Grid-Independence and Comparison with Measurements: Figure 9 shows a comparison of temperature contours with 300,000 and 1,200,000 grid points. Results are comparable with each other. A quantitative comparison shows differences of less than 5% in the results. Figure 10 shows the radial-temperature profiles at two axial locations, z/d_f=0.87 and z/d_f=0.2, and agreement between the data and predictions is quite reasonable. Generally the difference between the measurements and predictions is of the order of 10-12%, although larger differences exist close to the location of the primary air-injection (nearly 20%). Figure 10 shows comparison between measurements and predictions of the radial velocity, axial velocity and tangential velocity at two axial locations, z/d_f=0.2 and 0.87. Measurements have been made using Particle Image Velocimetry (PIV). The radial velocity predictions and measurements are nearly in perfect agreement with each other. The axial velocity measurements show generally good agreement except immediately below the primary air-injection site, where differences as large as 30-50% can be observed for r/d_f<0.4. However, for r/d_f>0.4, the differences between predictions and measurements are small. The tangential velocity predictions also show excellent agreement with measurements. The radial velocity predictions and measurements show that the entrainment of the annular air stream into the cavity region is primarily confined to the region near the afterbody, and purging of the combustion air from the cavity occurs closer to the forebody.

The tangential velocity measurements and predictions show the important role of swirl on the fluid dynamics. Magnitudes of peak tangential velocities are nearly 30% of the axial velocities and are comparable to the radial velocities.

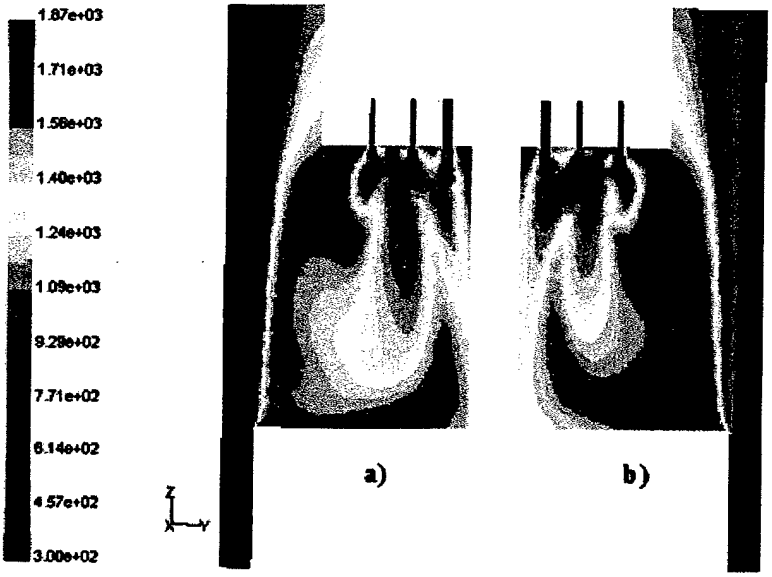

Figure 9: Contours of Temperature calculated by (a) 1,200,000 and (b) 300,000 grid elements (30° Swirl Injection, $\phi_p = 0.88$)

Effect of Swirl Injection: Figure 11 shows the predicted velocity vectors and temperature contours for straight and swirl injection. With swirl, the cavity vortex is shifted closer to the afterbody, and higher temperatures are seen in both the forebody and afterbody regions. The swirl injection promotes circumferential mixing and enhances both the heat release and the uniformity of temperature distributions. This is a desired goal. Figure 12 shows PIV measurements made under similar flow rate conditions (but without reactions) for straight injection and swirl injection, respectively. The PIV measurements also show that with swirl injection, the cavity vortex is moved closer to the afterbody. This observation agrees with the predictions. Quantitative comparisons between the velocity vectors in Figures 11 and 12 have not been made, since Figure 12 correspond to non-reacting conditions.

Effect of Alternate Configurations: Figure 13 shows results of computational studies exploring alternate configurations. Although a number of different configurations were studied, results of only two configurations are shown. The left figure shows injection from the forebody and the afterbody leading to the creation of double longitudinal roll cells. The figure on the right shows injection from the spindle and both the forebody and afterbody, leading to the generation of transverse double-rolls. For this configuration, reacting flow predictions of the temperature distribution are presented in the bottom figure, and show very uniform temperature distributions. In this case, fuel injection was done only from the forebody, and the high temperature gases are transported to the afterbody vortex by the annular flow. This configuration, with fuel injection from the foerbody and the afterbody, is likely to provide the most uniform temperature distributions in the cavity region. It is, therefore, recommended that this configuration be explored experimentally.

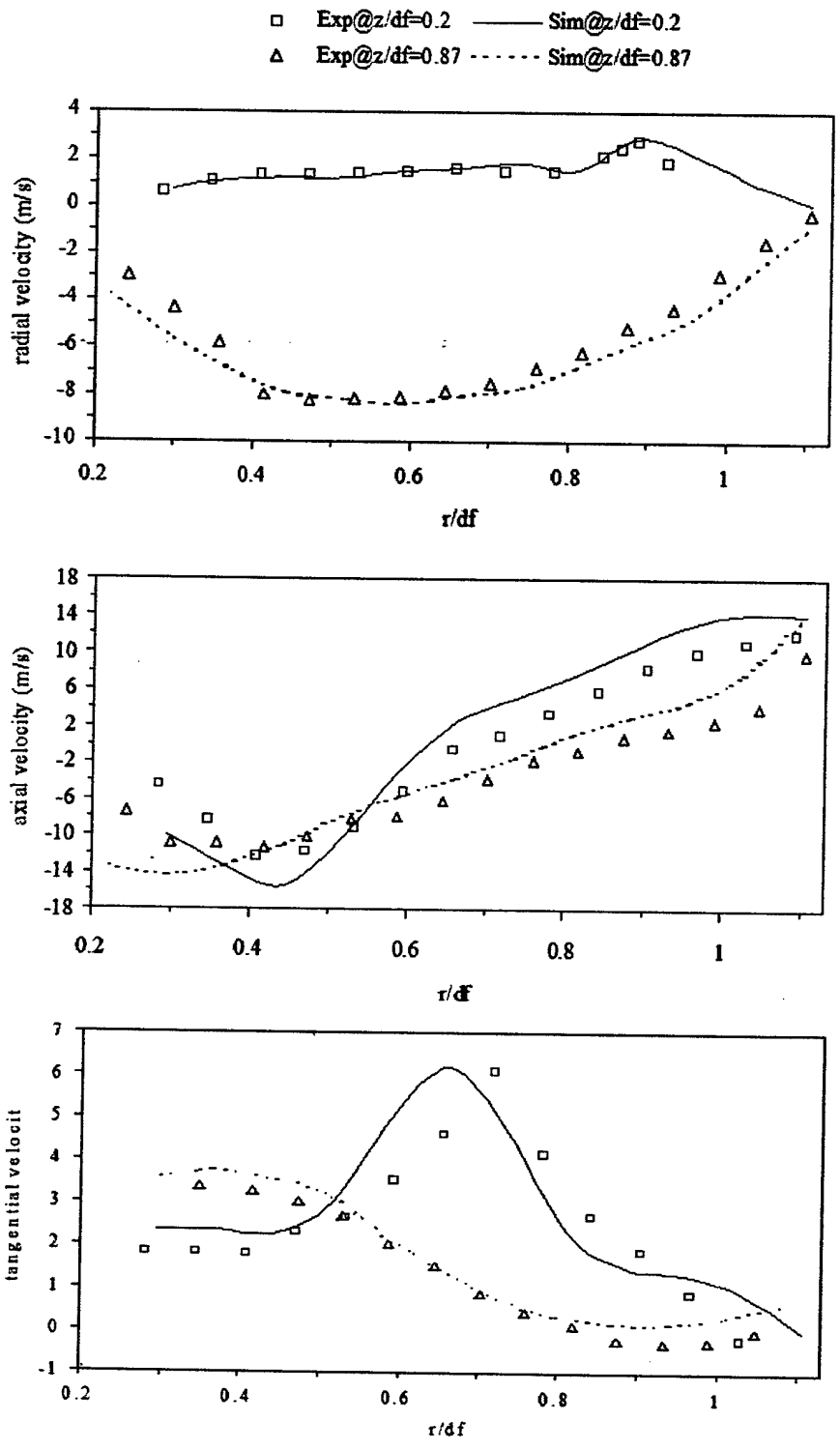

Figure 10: Radial, Axial and Tangential Velocity profiles for $\phi_p = 0.88$ (Swirl Injection)

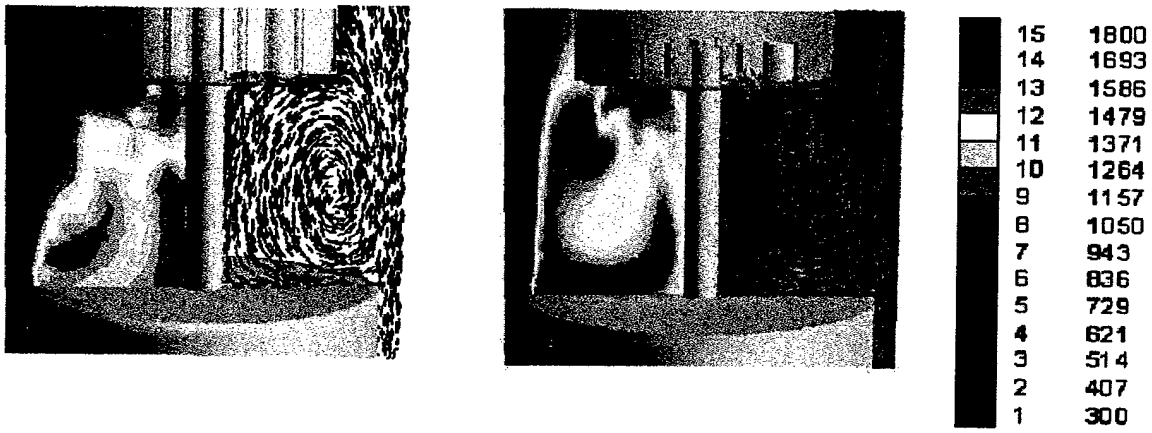

Figure 11: Temperature contours and velocity vectors (computed) for $\phi_p = 0.88$ at annular velocity of 15m/s: Straight Injection (left), Swirl Injection 30° (right)

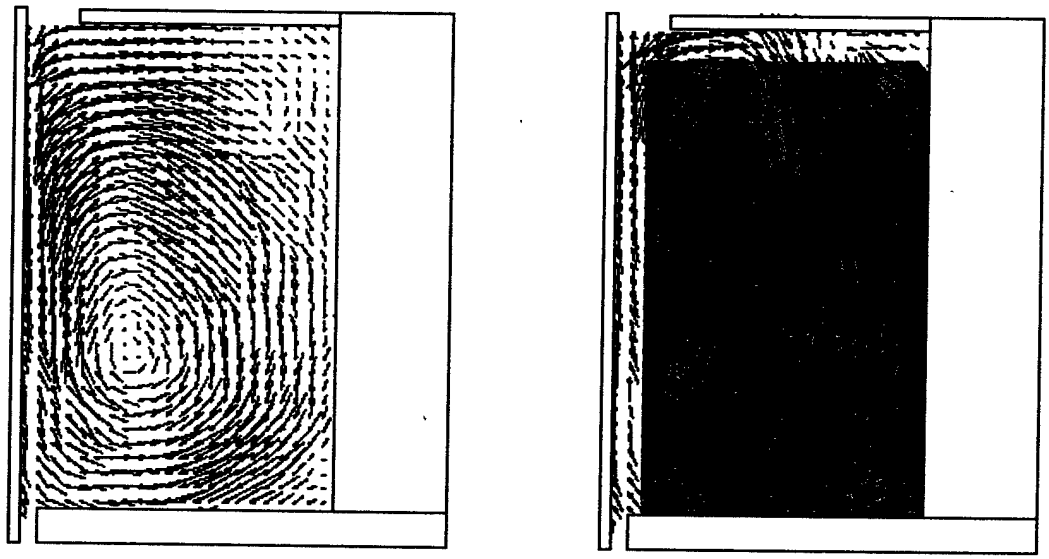

Figure 12: Measured velocity vector field: Straight Injection (left), Swirl Injection 30° (right)

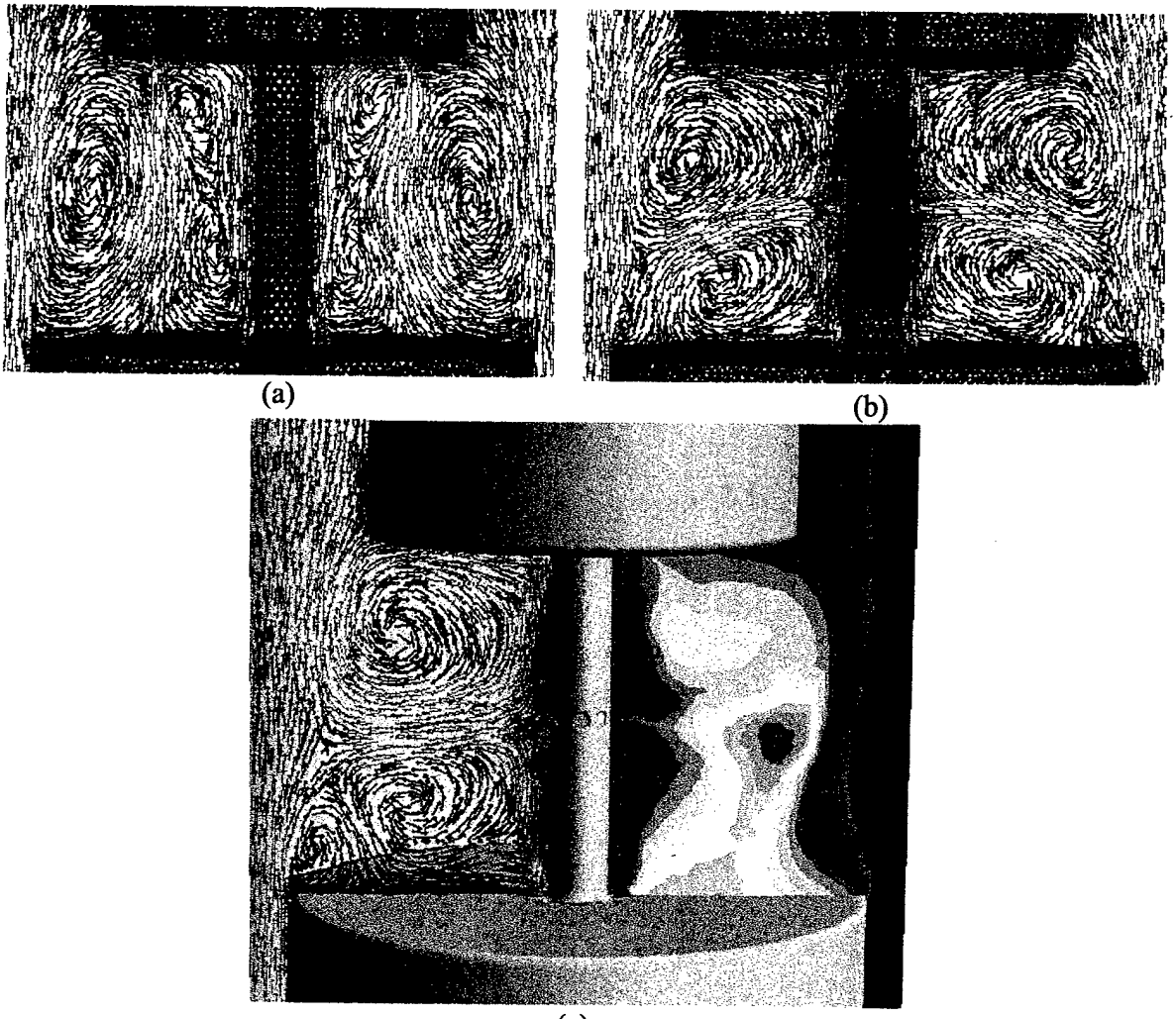

Figure 13: Alternate Configurations: (a) Dual-injection configuration from the forebody and afterbody; (b) Primary air injection from the spindle and both fore- and after-bodies; (c) Same as (b) showing temperature contours, fuel injection from forebody

Large Eddy Simulations (LES) for the Inner TV

Large Eddy Simulations in the inner-TV geometry are performed using a fractional step approach and a direct-Poisson solver. The temporal discretization is done using a second order-accurate Adams-Bashforth scheme. A fourth order-accurate finite difference scheme is used for the convective and diffusion terms. Following the dynamic mixed method of Zang et al. (1993), the subgrid stresses are decomposed into a resolvable part and an unresolvable part. The resolved part is the Galilean invariant form of a scale similarity model (Speziale, 1985). The dynamic Smagorinsky model is used for the unresolved part of the stress, and the dynamic coefficient is test filtered to avoid numerical instabilities.

The calculations are done on a Cartesian grid, and the immersed boundary method is used to incorporate the complex cylindrical geometry of the TV combustor (Tyagi and Acharya, 2001, 2003). In the immersed boundary method, the complex geometrical features are incorporated by

adding a forcing function in the governing equations. The forcing function is zero everywhere except at the surface, where the influence of the solid boundaries is assigned.

The instantaneous velocity vectors and the spanwise component of vorticity ω_y are presented at the meridional planes $\theta = 0°$ and 180° in Figure 14. The distribution of vorticity is nearly anti-symmetrical at these planes, as expected. At all time instances, the distribution of vorticity at the meridional planes $\theta = 0°$ and 180° differs significantly from the distribution at $\theta = 90°$. All of these planes pass through the centerplane of the fuel injectors and indicate the importance of 3-dimensional effects. The instantaneous center of the TV at $\theta = 90°$ is near the afterbody, while the center of TV at $\theta = 0°$ and 180° is near the cavity center. Therefore, the TV at this instance has a toroidal structure, with the center shifting spatially and temporally. Highest vorticity and mixing are noted along the edges of the TV and in the annular air stream. The cavity flow is ingested into the annular flow near the forebody, while the annular flow is entrained into the cavity primarily in the vicinity of the afterbody. This cross-mixing between the annular flow and the cavity flow is essential for sustaining a stable flame in the cavity. Periodic shedding of vortices is noted from the outward corner of the afterbody and could promote unsteady heat release behavior.

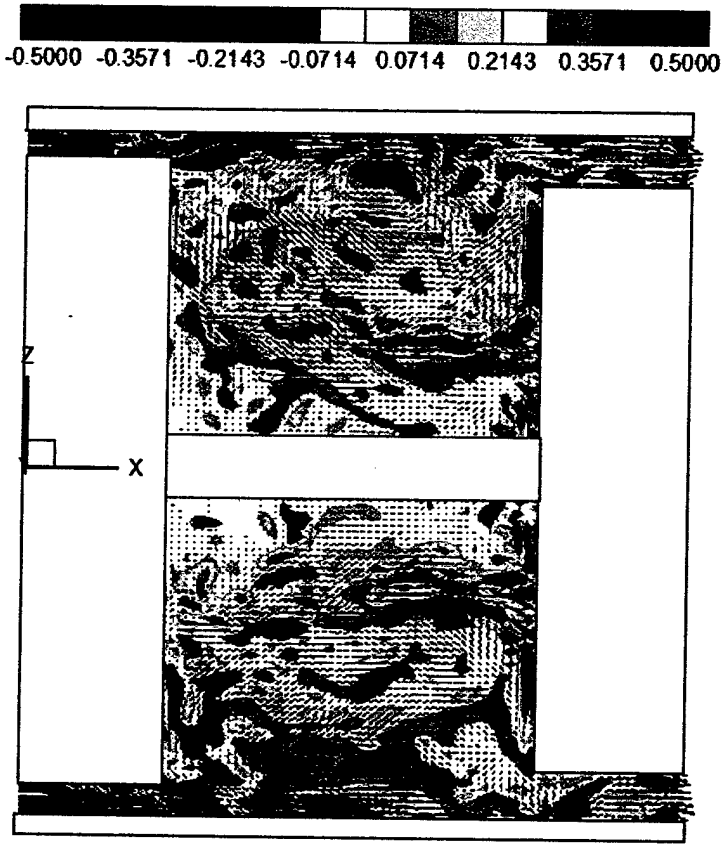

Figure 14: Instantaneous velocity vectors at $\theta = 0°$ and 180°.

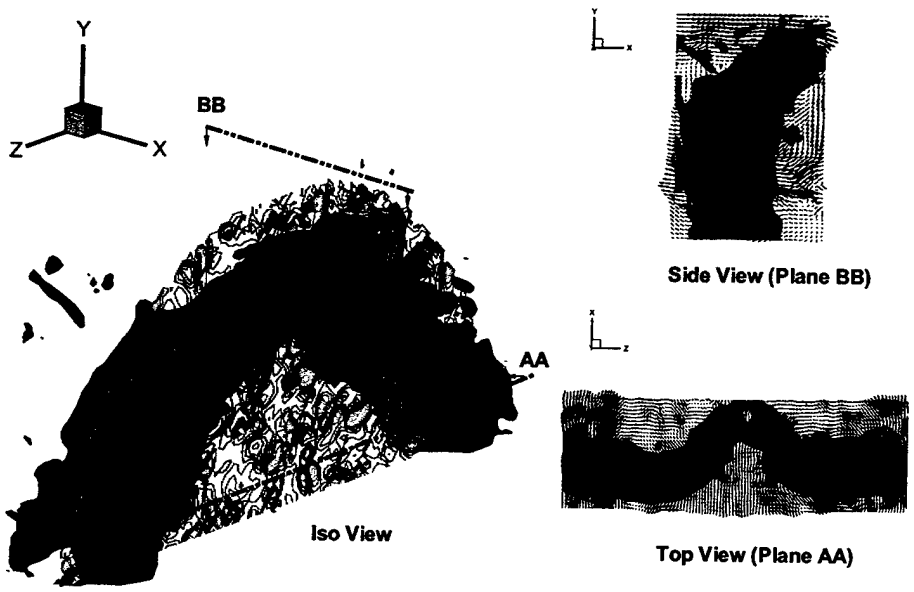

Iso-surface of low pressure in the core of trapped vortex

Streamwise component of vorticity contours at X/D plane through the doughnut shaped surface

Insets: Top and Side views of the iso-surface with velocity vectors on the plane

Figure 15: Iso-surface of pressure in the cavity

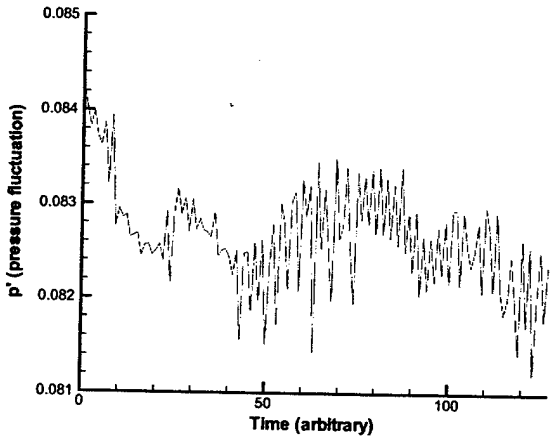

Figure 16: Large and small scale variations of the pressure fluctuations during the transient at $\theta = 0°$, R ~ 14 D, X/D = 39

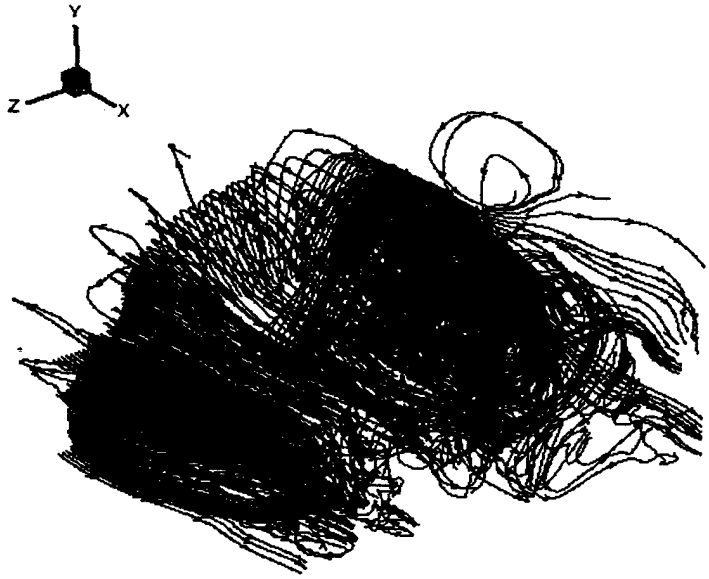

Figure 17: Streamtraces representing the toroidal vortex in the cavity

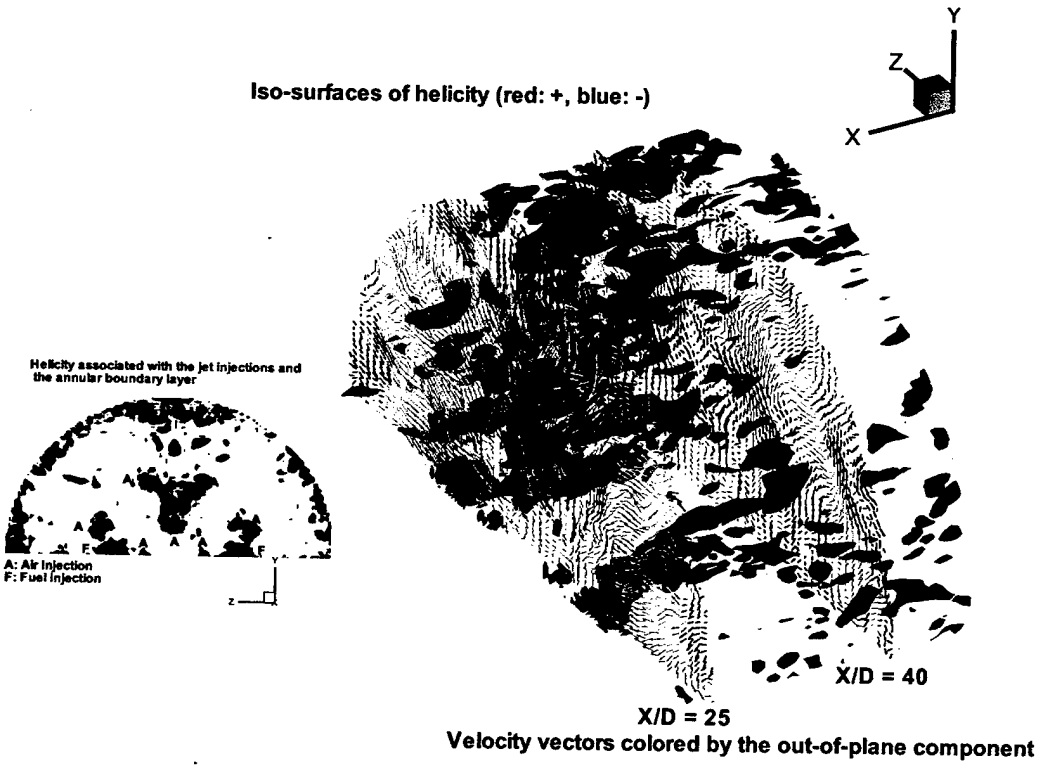

Figure 18: Details of the flowfield near the injection jet from the afterbody

An iso-surface of a low-pressure level around the core of trapped vortex is visualized as a doughnut-shaped tube in the cavity (Figure 15). The details of the flow field around this surface clearly shows the velocity vectors wrapping around the surface. A typical signature of pressure fluctuation at meridional plane $\theta = 0°$ and an axial location in front of the fuel injection shows both large and small scale variations (Figure 16). Clearly, the small-scale fluctuations depict the turbulent diffusion at this location, and the large-scale variability can be associated with coherent motions of the TV inside the cavity.

Streamtraces in the cavity are presented in Figure 17, and clearly show the existence of a toroidal vortex structure in the cavity. To identify the vortical structures associated with the injection jets, the helicity (defined as scalar product between vorticity and velocity) is used (Figure 18). Positive and negative tubes of iso-helicity surfaces can be identified inside the cavity and in the boundary layer regions along the outer shell of the cavity. Two cross-stream planes are presented to show the velocity vectors around these injection jets. Radial ingestion of the annular fluid into the cavity is seen along these jets.

B. Outer TV Configuration

The schematic of the outer TV configuration was shown in Figure 3. Two different air-injection configurations (Figure 19) from the afterbody were investigated. In one, the primary air was injected from the outer corner of the afterbody, leading to a single vortex in the cavity. In the second configuration, the air was injected coaxially with the fuel and is likely to lead to a double-vortex configuration. The fuel injection location is unchanged for both configurations.

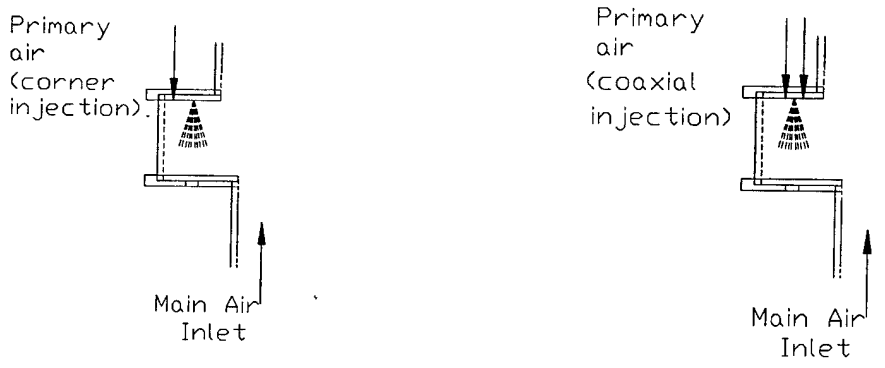

(a) (b)

Figure 19. Two configurations of primary air injection into the cavity (a) corner air injection and (b) coaxial air injection

Measured Emissions

Emissions measurements for different main air flow rates and cavity air flow rates are presented in Fig. 20-22. Figure 20 shows the distributions of NO_x, combustion efficiency (η), carbon monoxide (CO), and stack temperature distribution for a fixed primary (or cavity) equivalence ratio, ϕ_p, of 1.27. The primary fuel flow rate and airflow rates for this condition are 1.8 gph and 7 scfm respectively. The primary air is injected coaxially to the fuel spray into the cavity. Measurements are taken for this fixed primary equivalence ratio and varying main flow rates ranging from 30 scfm to 100 scfm. The combustion efficiency is seen to increase from 89% for low main air flow to a maximum value of 92% at 100 scfm main supply air. NO_x emissions

for these flowrates decrease continuously as the main flow is increased - from a maximum value of 6 ppm at 30 scfm to nearly 0 ppm (not detectable by the current NOx analyzer) at the highest airflow tested. As expected, exit stack temperatures decrease as the main air supply is increased.

The measurements are repeated for corner air injection in order to compare the effect of the primary air injection location on the combustion performance. The NO_x emissions, under similar conditions, range from a high value of 20 ppm at a low main air flowrate of 40 scfm to a minimum of 8 ppm at the highest flowrate of 100 scfm (see Fig. 21). When compared to the coaxial air injection, the corner primary air injection has higher NO_x emissions, with values as high as 20 ppm at the exit of the combustor (when compared to 6 ppm in the case of coaxial combustion). The corner injection strengthens the vortex formation inside the cavity with the formation of single vortex, whereas the coaxial air injection gives double vortex formation, with a small vortex forming inside the cavity in addition to the main vortex. Also, CO emissions are much higher in the case of corner primary air injection as compared to coaxial air injection, with emissions reaching as high as 550 ppm.

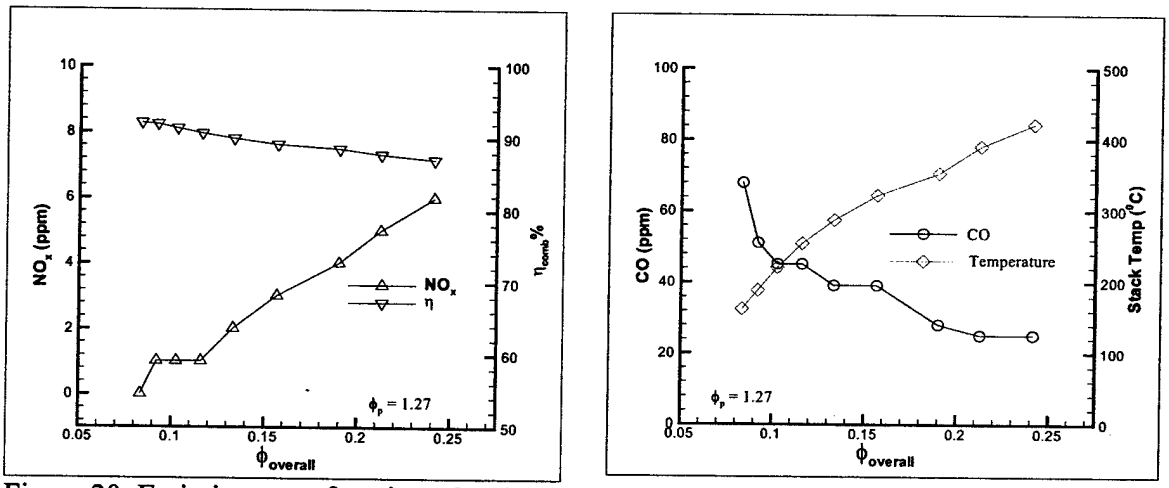

Figure 20: Emissions as a function of main airflow rate for coaxial primary air injection.

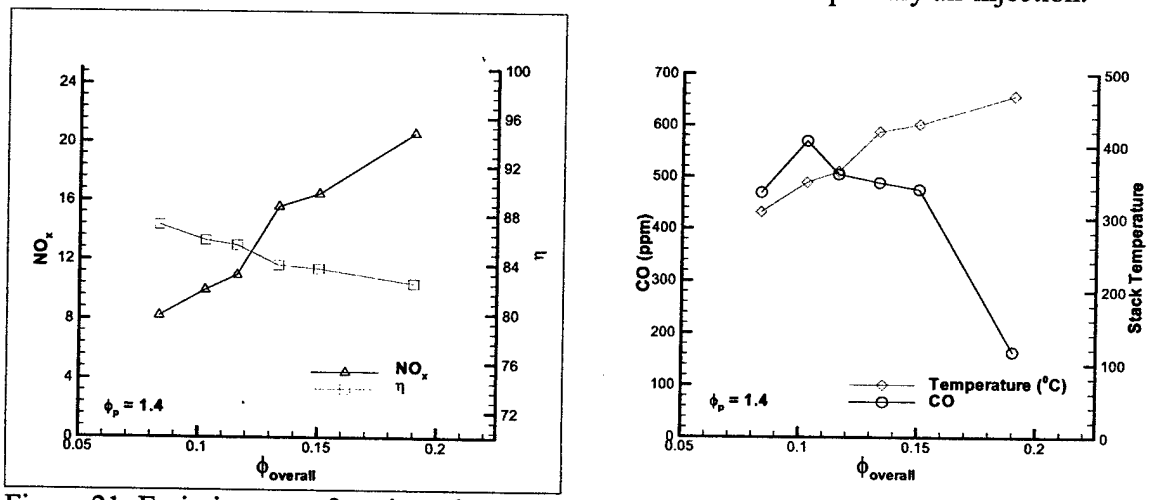

Figure 21: Emissions as a function of overall equivalence ratio for corner primary air injection.

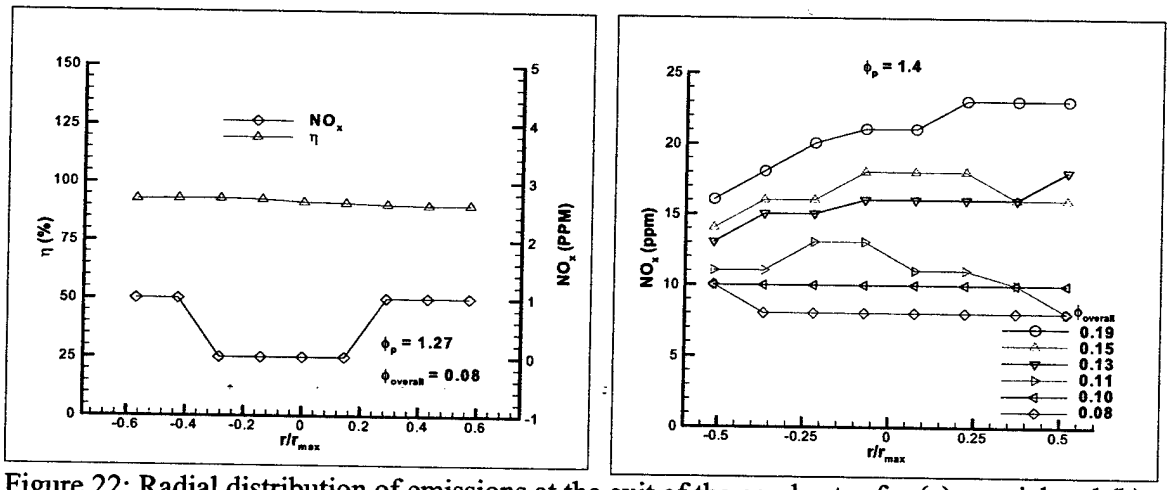

Figure 22: Radial distribution of emissions at the exit of the combustor for (a) coaxial and (b) corner primary air injection.

Figure 22 gives the radial distribution of emissions at the exit of the combustor. The distributions are fairly uniform along the exit radius and show slight variation at low main flowrates (see Fig. 22b). This radial variation in NOx is due to the use of three circumferentially-distributed fuel injectors located inside the cavity that give rise to relatively cold regions between the spray injection locations at the exit of the combustor. This variation disappears for higher main air supply due to greater mixing, and the exit conditions are uniform throughout the region. Combustion efficiencies close to 95% are recorded for coaxial air injection, with NO_x emissions close to 25 ppm (at $\phi_{overall}$=0.08). NOx emissions were lower with corner injection and single digit (8ppm) NOx was recorded at $\phi_{overall}$=0.08.

Measured Temperature Distribution

Temperature measurements are taken inside the cavity at three combustor axial locations and at radial increments of 0.25". Representative plots of temperature distributions for coaxial primary air injections are presented in Figs. 23(a and b). Two primary air injections of 7 scfm (ϕ_p = 1.27) and 10 scfm (ϕ_p = 0.89), respectively, are presented in these plots. Higher temperatures, with a maximum of 1350 K, are observed for 10 scfm cavity air flowrate when compared to 7 scfm airflow. The trough in the temperature near the cavity top and bottom is due to the cold fuel injection into the cavity. Peak temperatures are measured near the center of the cavity, where the mixing is expected to be maximum, resulting in higher temperature. Visual observations of the flame show a strong vortex at the edge of the cavity, with blue flame representing clean (non-sooty) combustion. Roquemore (2003) used struts in the main flow that create low pressure zones in their wake for passage of hot products helping in main combustion. At higher primary air injection of 10 scfm, the temperature distribution inside the cavity is quite uniform, with temperatures of 1200 K throughout the cavity. The temperature distribution suggests better mixing and combustion inside the cavity for this primary air injection (ϕ_p = 0.89).

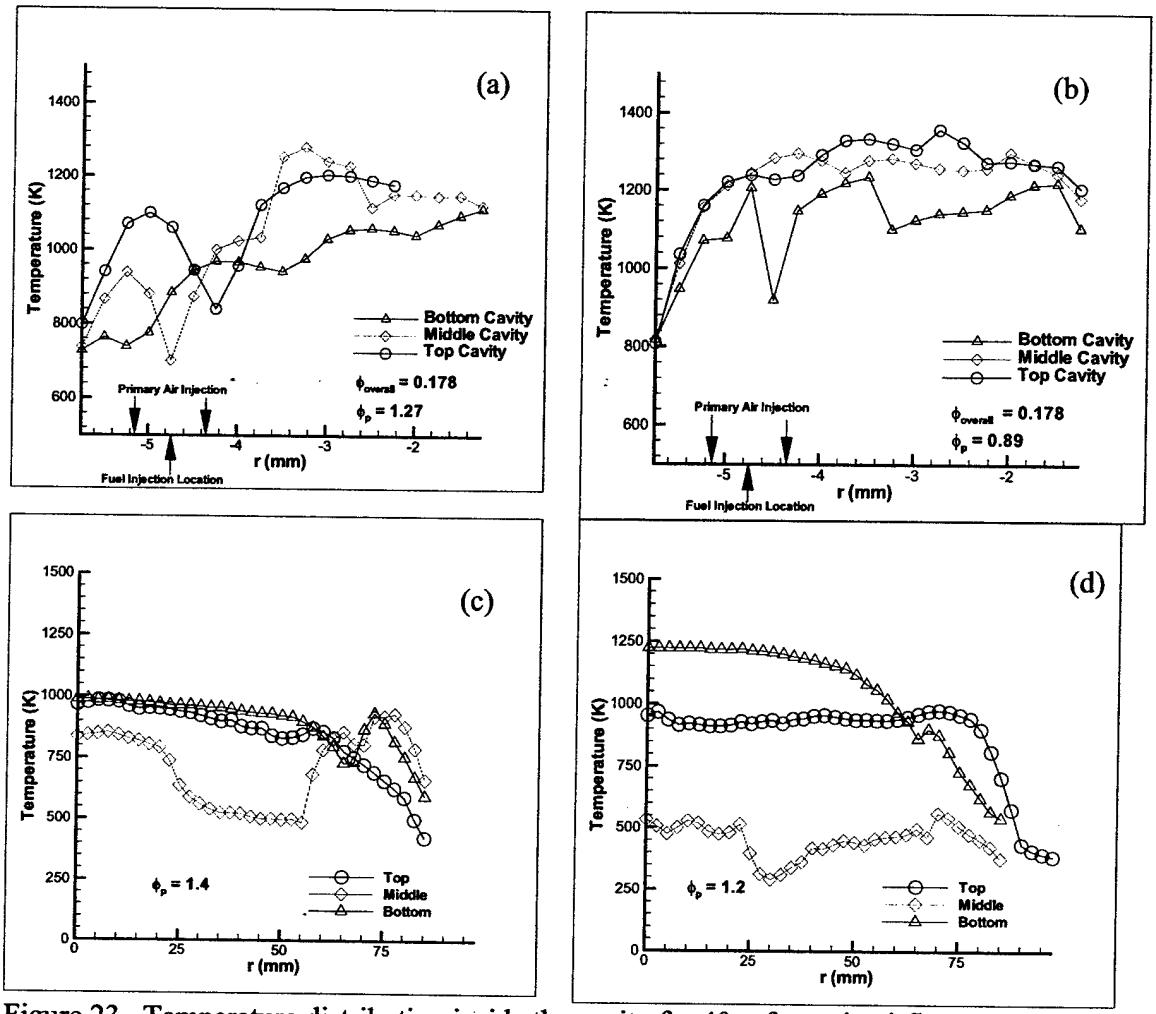

Figure 23. Temperature distribution inside the cavity for 40 scfm main airflow and primary equivalence ratio (coaxial) ϕ_p of (a) 1.27 and (b) 0.89 and corner ϕ_p of (c) 1.4 and (d) 1.2.

Lean Blow Out

Lean blow out conditions were measured by increasing the primary air into the cavity until the flame blow out occurs inside the cavity. During the process, both main airflow through the combustor and the fuel flow rate into the cavity are kept constant varying only the primary air into the cavity. Lean blow out measurements are then repeated by varying the main airflow rates for both coaxial primary injection and corner air injection. Figure 24 shows the LBO limits for both corner primary air injection and coaxial air injection. Lean blow out limits are lower in the case of corner injection as the location of air injection is far away from the fuel injection inside the cavity. Overall LBO limit as low as 0.07 is achieved for corner air injections inside the cavity. Lean blow out limits in terms of cavity equivalence ratio are 0.75 and 0.3 for coaxial and corner primary air injection respectively. As the cavity flame is shielded from the main air supply, the overall LBO limit can be very low as the main flow is increased without disrupting the cavity combustion.

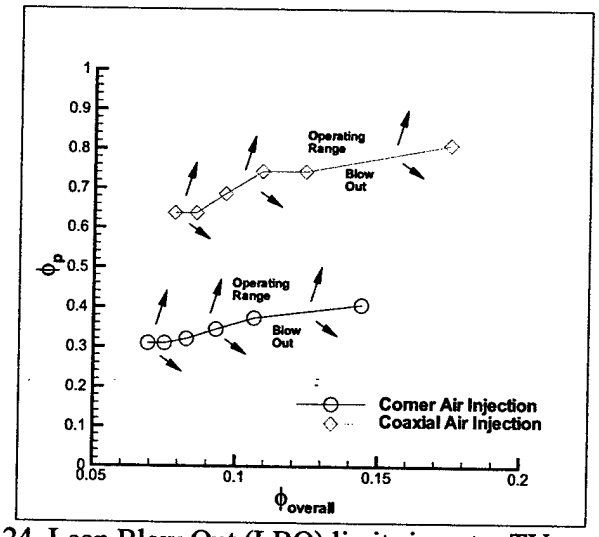

Figure 24 Lean Blow Out (LBO) limits in outer TV combustor

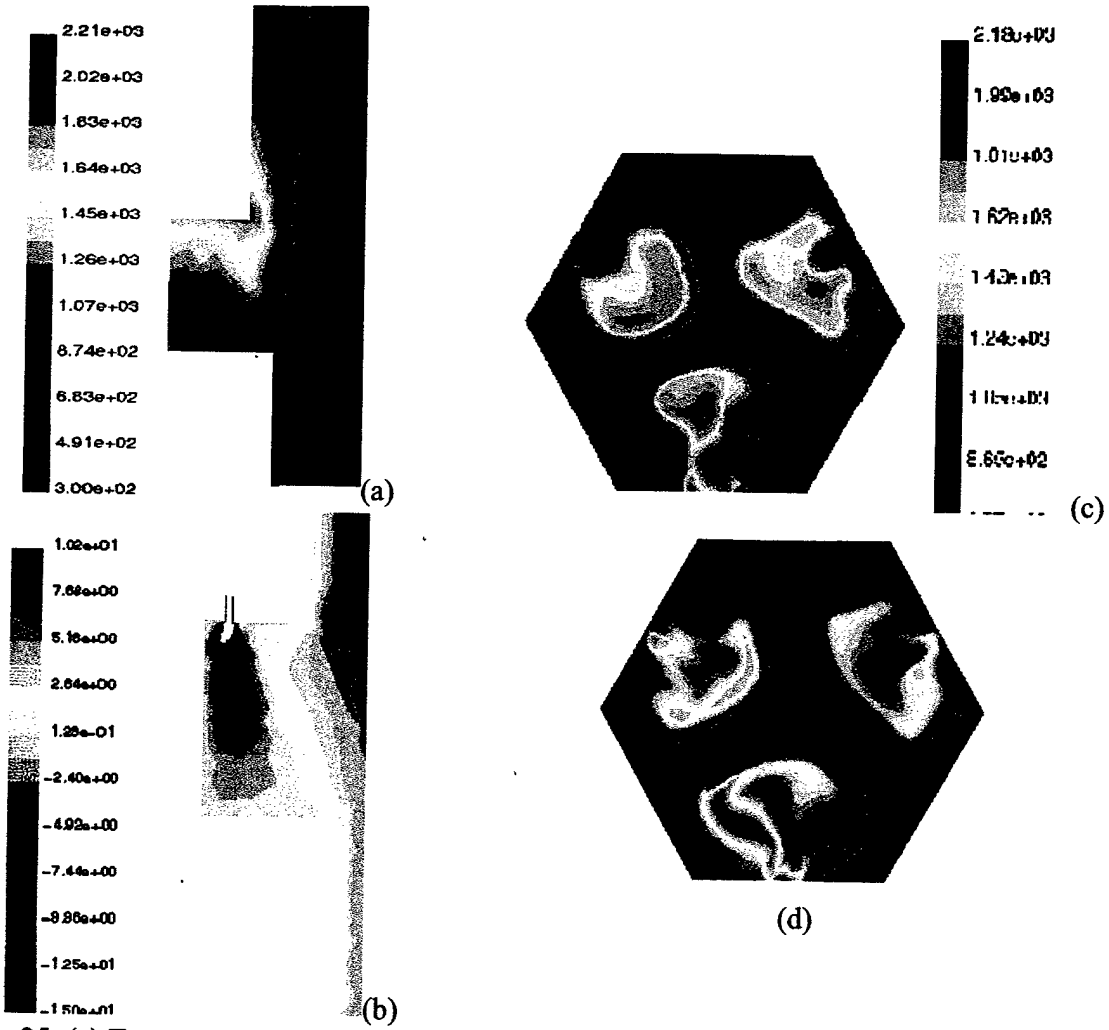

Figure 25: (a) Temperature (K) (b) axial velocity (m/s) (c) Temperature at a horizontal cross-section near after-body (K) (d) Temperature at a horizontal cross-section near mid-cavity

Computations

For the inner cavity, detailed RANS computations were conducted for a variety of flow conditions. Figure 25 shows a typical computation at a ϕ_p =1.98. Shown in the figure are the temperature contours in a vertical plane, the axial velocity contour in a vertical plane, and the temperature contours at two horizontal cross-section planes. The vertical cross-section temperature contours show that some of the combustion is taking place outside the cavity (note that fuel is injected only into the cavity in these simulations). The horizontal cross-section temperature contours (Figs 25 c and 25d) show that the circumferential mixing is inadequate and that there are cold spots between the fuel injectors. This non-uniformity in the circumferential temperature distribution indicates that the swirl injection would be desirable in this configuration.

VI. MICRO-FUEL INJECTOR-DESIGN AND FABRICATION

Objectives

The objective of this project was to design micro fuel injectors with micro-nozzles and integrated micro-swirl channels for both air and fuel in order to improve atomization and mixing of the fuel–air mixture. Three approaches were investigated:

- hybrid fabrication of a metal fuel injector array;
- development of processes for producing ceramic micro fuel injector components;
- use of a multi-layer microfabrication sequence to produce single, integrated fuel injectors.

Each of these tasks presented significant challenges in the development of fabrication tools and techniques. An assembled array of metal fuel injectors is almost complete. Work is continuing in all three areas.

Design

The core of the design for improving mixing of the fuel and air was the placement of microscale swirler structures at the entrance and exit of a micro-nozzle. The fuel passes through the swirler at the entrance, through the micro-nozzle, and mixes with high pressure air passing through the swirler at the exit to the nozzle. A schematic of the swirler at the nozzle entrance is shown in Figure 26. The combination of vorticity introduced by the swirlers and fine atomization with the micro-nozzle is expected to produce better mixing and lead to better combustion.

Packaging of the micro-swirlers and micro-nozzle to realize the configuration in Figure 27 required additional considerations. Three different reservoirs for the containment of the fuel, high-pressure air, and low-pressure air were necessary. The complementary, low pressure air was needed to maintain the stoichiometry of the fuel-air mixture in order to ensure complete combustion. Reservoirs also reduced the number of connection sites for supply lines needed for each of the three fluids. Decreasing the need for individual connectors for each fluid for each micro-injector reduced the overall size of the array of micro-injectors. The prototype array had one fuel line and four air supply lines, two for each pressure, for the array of four micro-injectors.

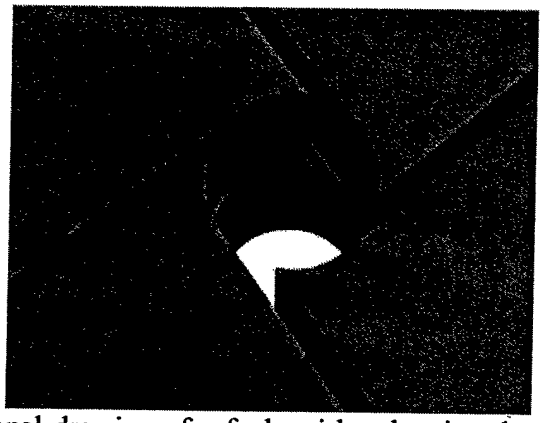

Figure 26. Three-dimensional drawing of a fuel swirler showing the channels flowing into the swirl chamber. Fluid enters the swirl chamber tangentially, swirls, and exits through the micro-nozzle at the bottom.

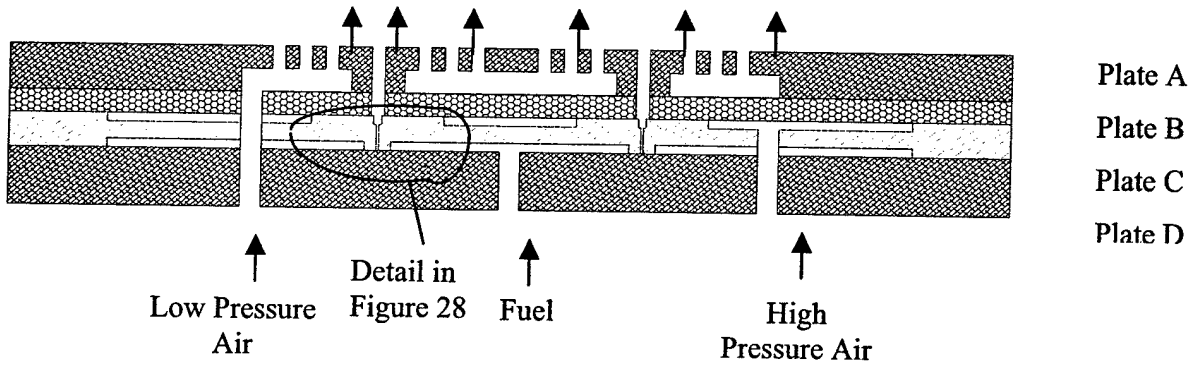

Figure 27. Cross-section of two fuel injector nozzles. Arrows indicate the direction of fluid movement.

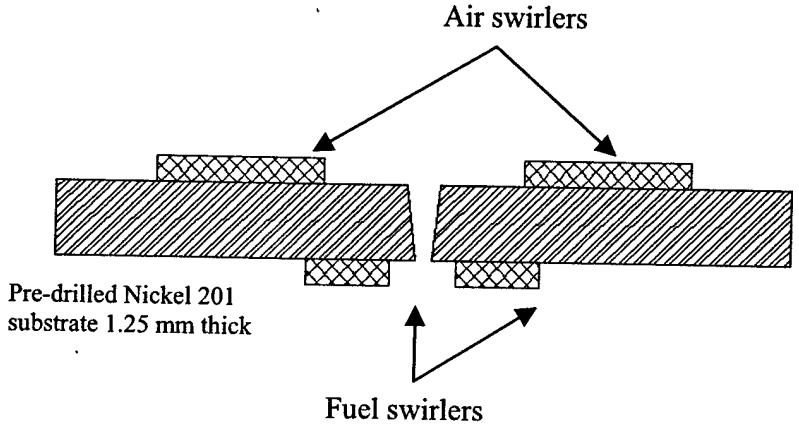

Figure 28. Cross-sectional view of swirlers formed on both sides of the plunge EDM-drilled connecting hole.

A multi-plate structure was chosen for the prototype metal micro fuel injector. A cross-sectional view of the four plates is presented in Figure 27. Each plate required precision machining for integration of the microstructures and fuel injector operation, while Plate C was a substrate for the microfabricated swirlers for the fuel and air on each side, respectively. Figure 28 shows a cross–sectional view of the relative locations of the micromachined swirlers on each side of Plate C and a top view of the fuel and air swirlers is given in Figure 29. The microfabricated structures were nominally 75 μm tall. Plate B capped the air-side microchannels and Plate D capped the fuel-side microchannels. Plate A defined outlets to the combustor for the air/fuel mixture and the complementary low-pressure air.

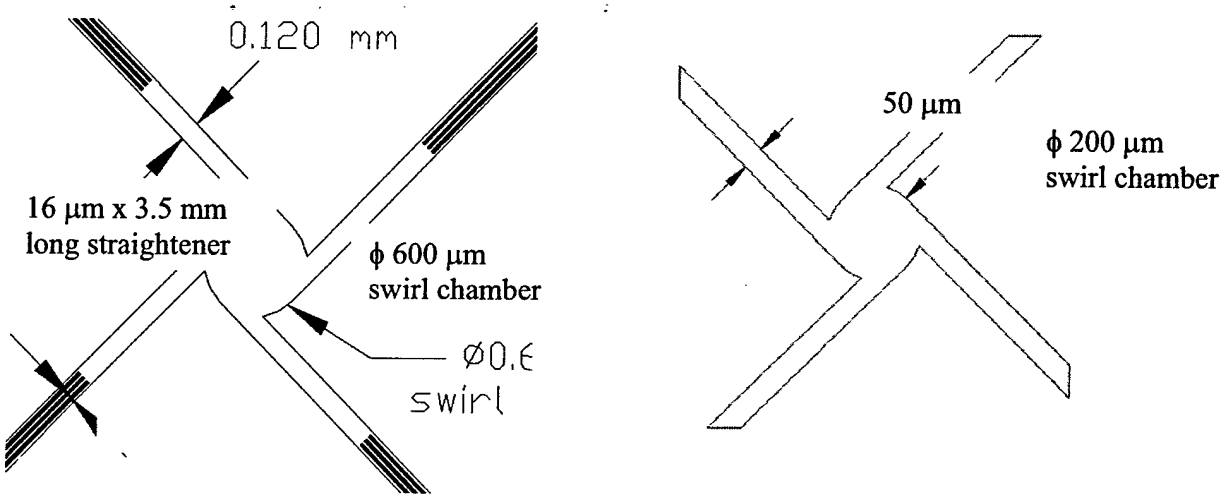

Figure 29. Illustration of a microfabricated (a) air swirler consisting of four 18 μm wide microchannels created by three 16 μm wide electroplated nickel fins on each leg and (b) fuel swirler composed of four 50 μm wide and 1 mm long channels. The high-pressure fluid enters the swirler from beyond the microchannels, travels through the straighteners, and exits through a hole in a direction perpendicular to the swirler plane. The fluids will mix in a co-rotating manner. In the prototype devices the fins in the channel were eliminated.

Fabrication – Metal Fuel Injectors

Mechanical fastening was selected as the means of assembling the prototype metal fuel injector array. This allowed separate fabrication processes for the different plates and the potential for evaluation of sealing between each pair of plates but introduced through-holes with additional sealing requirements and increased the complexity of the structure. Plates A, B, and D were produced using only traditional machining, while Plate C required the aligned microfabrication of the swirler structures, ports for air, and through-holes for screws on both sides of the plate. The following sections review the critical issues in each step.

Material Selection: Maximum operating conditions of the prototype fuel injector were specified as 500°C and 1 MPa. To avoid plate deflection, the yield strength and modulus of elasticity of each plate were selected to operate at sustained elevated temperatures. Plate C was Nickel 201

due to its common application as a substrate in electroplating nickel and its ability to maintain acceptable mechanical properties up to 500°C. Plate A and Plate B were Inconel 600 due to its robustness in high-temperature applications. Stainless steel was used for Plate D because the stainless steel fluid connectors could be welded to it and it had good resistance to corrosion at elevated temperatures.

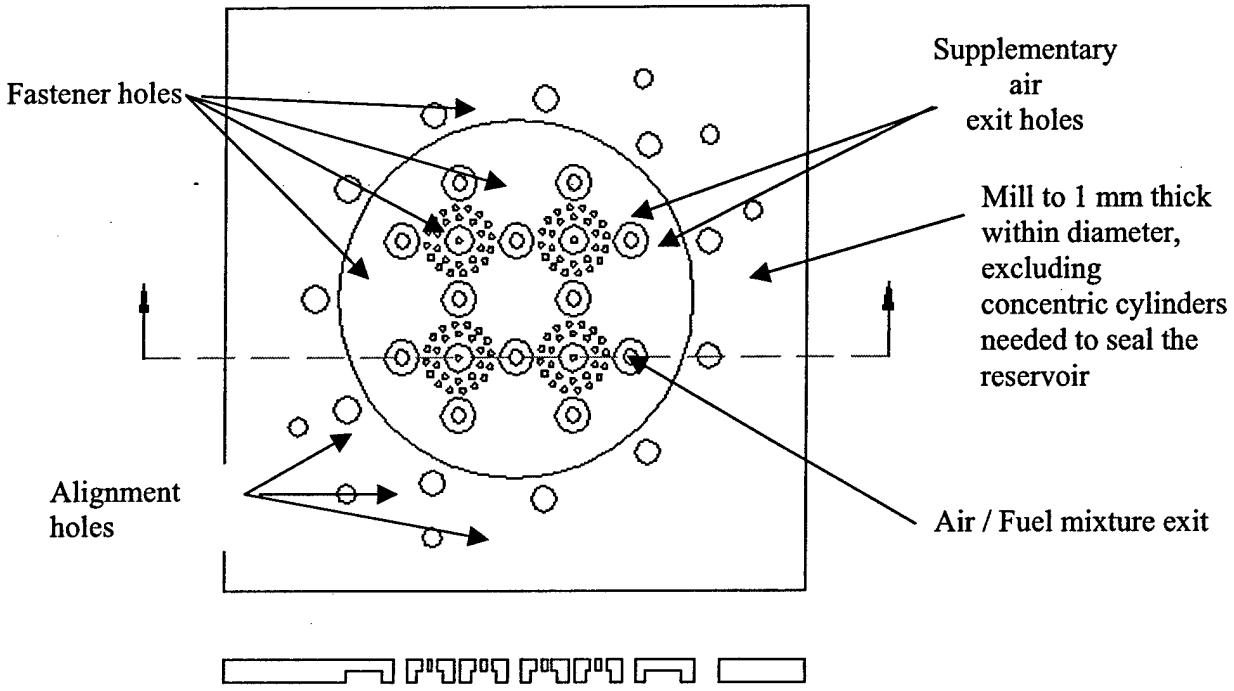

Figure 30. CAD drawing of precision milling and drilling on Plate A. Note the cross-sectional view along the indicated section line.

Plates A, B, and D - Traditional machining-alignment holes were drilled through each set of four plates simultaneously, to tolerances as tight as 10 μm, using a CNC drill. This simultaneous drilling reduced burr formation and misalignment. Individual hole patterns for the different plates were then drilled separately, using the alignment holes as points of reference. A larger tolerance was allowed for the location and drilling of the larger fastener holes. The relative positions and number of fasteners were determined by minimizing the plate deflections between fasteners. Due to the high inlet pressures of the fuel and air on either side of Plate C, the maximum bolt separation was 20 mm.

Milling was required on the 2 mm thick Plate A in order to create the 1 mm deep upper reservoir, as indicated in Figure 30. The reservoir provides a path for complementary air to flow into the secondary combustion chamber along with the fuel-air mixture. Cylindrical ridges were left around the fastener holes and air/fuel mixture outlets to prevent leakage and premature mixing with the low pressure air. The finished plate is shown in Figure 31.

Plate B included the 1 mm diameter air/fuel orifices and low-pressure air inlets. It also served as the cap to seal the air swirler microchannels. Figure 32 shows the completed Plate B. Housing the compression fittings for all of the supply lines was one of the functions of Plate D (Figure 33). Traditional machining was used to drill and tap all of the holes necessary to

accommodate the compression fittings. The fittings were welded to the plate, and the top surface was ground for flatness and polished to obtain low surface roughness on the side mating with Plate C. That side sealed the fuel swirler microchannels on Plate C.

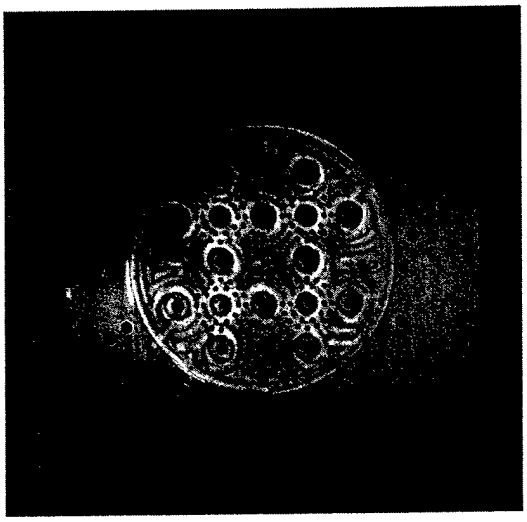

Figure 31. Finished Plate A, showing the key features on the plate.

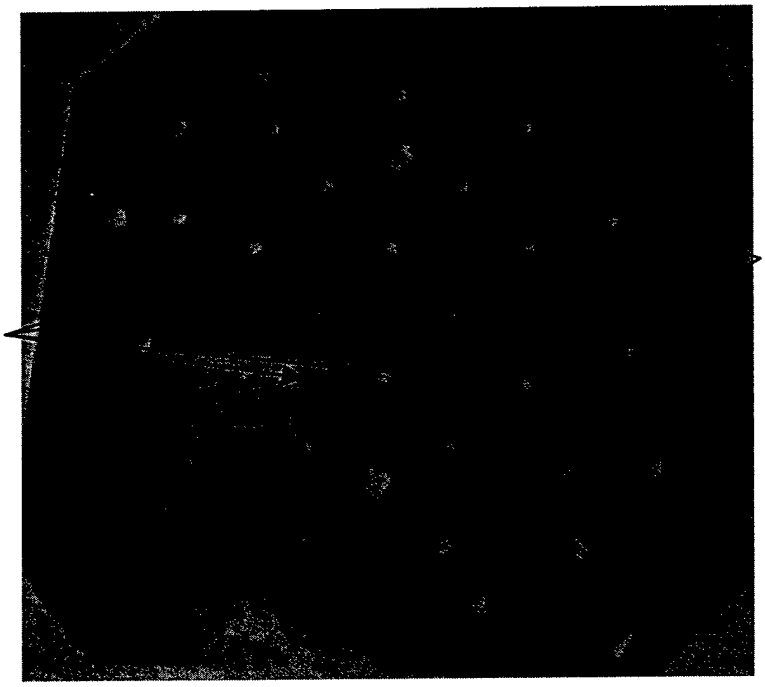

Figure 32. Completed Plate B. This seals the air swirlers and forms the bottom of the low pressure air reservoir.

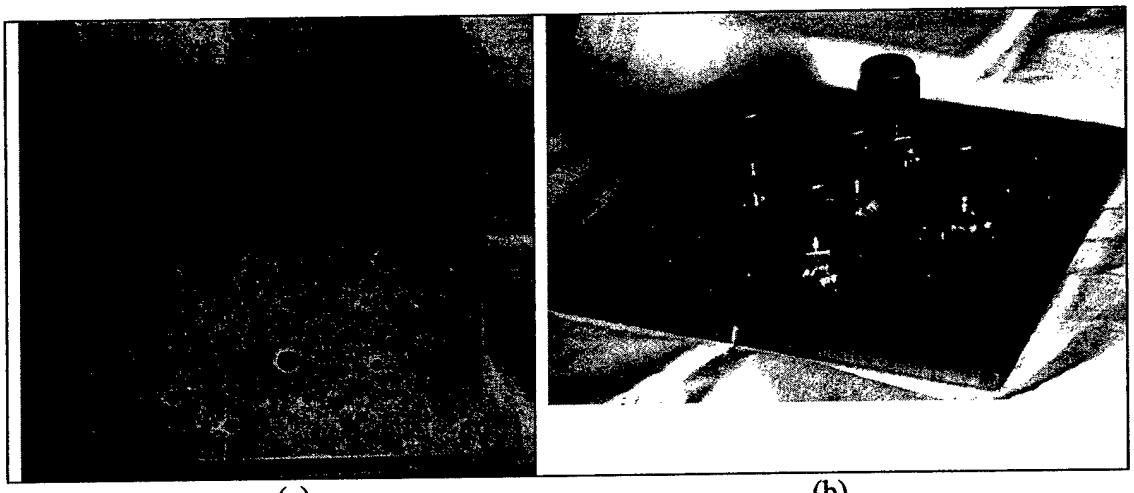

(a) (b)

Figure 33. Two views of the completed Plate D. (a) Fuel side showing the smooth surface for sealing the fuel swirlers and the pattern of alignment, fastener, and supply holes; and (b) Back side showing the compression fittings for the supply hoses, with the fuel inlet in the center.

Flatness, thickness variation, and surface roughness of all interfacing plate surfaces were machined to tight tolerances. Sealing between plates was accomplished by precision surface finishing for a peak-to-peak surface roughness of 0.5 μm and leveled to within 1 μm. Thickness variation was minimized to within 2 μm to avoid inaccurate alignment between plates.

Plate C – Precision Machining and Micromachining: Three machining steps were necessary to fabricate Plate C. Key features are shown in the schematics of the mask layouts in Figure 27. First, plunge electro discharge machining (EDM) was used to make the micro-nozzles for the four fuel injectors. Second, traditional machining was used to drill fastener holes and through-holes for the high- and low-pressure air supplies. Finally, microfabrication with UV-LIGA was used to form the swirler structures and the conduits for the air supplies and fasteners. During the project, a parallel process reversing the second and third steps was initiated in response to some of the problems encountered with the original sequence.

For plate C, the port connecting the fuel swirl chamber to the air swirl chamber for each nozzle was machined using plunge EDM. A commercial vendor (Optimation, Inc., Midvale, UT) did the EDM machining. Nominally, the nozzle diameter ranged from 50 micrometers on the fuel side of the nickel substrate to 100 micrometers on the air side, giving a conical hole with an aspect ratio of 25 based on the fuel side diameter. Experienced EDM machinists typically obtain aspect ratios on the order of 17 (Jorgenson, 1999). Representative micro-nozzle entrance (fuel side) and exit (air side) holes are shown in Figure 35. The achieved aspect ratio was about 16, based on the smaller fuel side diameter. The alignment holes were used to define the datum for the EDM machining. The maximum lateral offset among all of the micro-nozzles was 160 μm, less than 16% of the 1 mm diameter opening for the fuel-air mixture in Plates B and A.

Traditional machining was used to locate and drill the fastener and air supply holes on Plate C. The tolerance for location and diameter of the holes was not as tight as on the micro-nozzles.

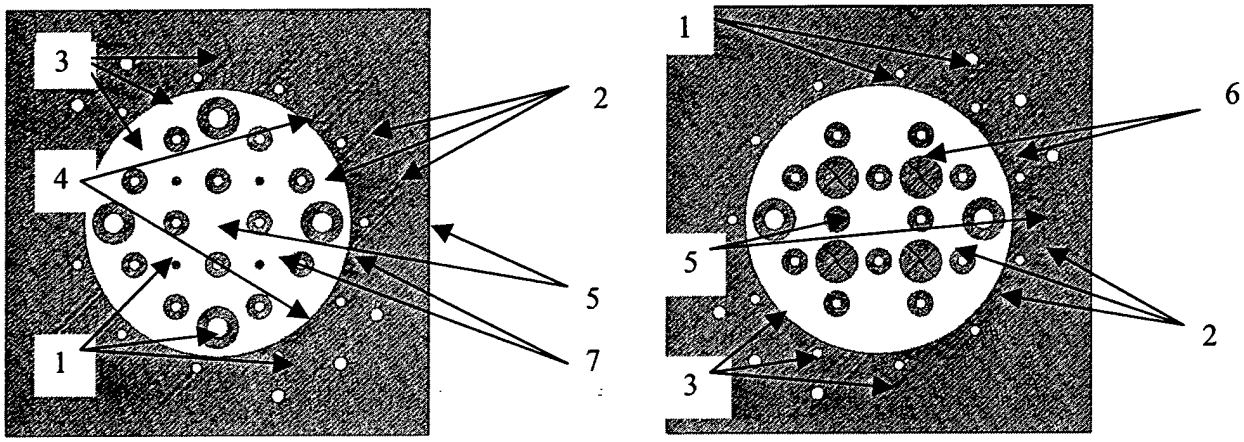

(a) (b)

Figure 34. CAD drawing of UV mask for (a) fuel and (b) air. The shaded areas will eventually be electroplated nickel. [1] are fastener holes, [2] are fastener holes with isolation cylinders to prevent leakage within the reservoirs. [3] are holes for alignment pins. [4] are high-pressure passages, and [5] are low-pressure routes. [6] are air swirlers and [7] are fuel swirlers.

The primary objective of third stage of the fabrication of Plate C was to create the swirler microchannels on each side of the plate. UV-LIGA, a high aspect ratio microfabrication process based on the patterning of deep UV resists and filling the patterns by electroplating, was selected as the process for generating these structures. This decision was based on the height of the final strucutures (75 μm) and relative availability of the X-ray source for LIGA microfabrication at the start of the project.

(a) (b)

Figure 35. Plunge EDM machined micro-nozzles through Plate C. (a) Fuel side opening approximately 80 micrometers in diameter, and (b) Air side exit diameter about 110 micrometers.

Figure 36 outlines the sequence of process steps used to fabricate the microstructures on each side of the plate. In step (a) 50 Å of chrome and 300 Å of gold were evaporated onto the sandblasted surface of the Nickel 201 substrate. The sandblasting and evaporated layers were needed to enhance adhesion between the resist and the nickel substrate. A negative, UV-sensitive resist, SU-8-25 (MicroChem, Newton, MA), was spin coated 90 μm thick onto the gold layer. UV exposure of the resist was accomplished at a dose of 450 mJ/cm^2, as shown by the arrows in step (a) (Ling, et al., 2000). The layout of the air and fuel UV masks is shown in Figure 34. The white areas on each mask identify the UV-exposed portion of the resist. The white circles of elements [1] - [5] also represent holes previously drilled through the substrate. The electroplated cylinders surrounding the fluid holes on the fuel mask allow the low- and high-pressure air to pass through the plate without mixing. The absence of similar high-pressure air cylinders on the air-side mask permits the high-pressure air to flow into the air-side reservoir. Step (b) in Figure 36 shows the device after the unexposed portions of the resist are removed by the developer. The UV-exposed structures are the negative of the final metal prototype. Optical photographs of typical resist structures are shown in Figure 37.

In order to ensure that all features are filled, the nickel is overplated (Step c). Surface finishing, including sanding and lapping, is needed to level the nickel structures at approximately 75 μm with a polished top surface. An overview of Plate C just after electroplating is presented in Figure 38. Step (d) shows the final nickel structures after the remaining resist layer is removed. Optical and SEM photographs of an electroplated swirler chamber and micro-nozzle are shown in Figure 39.

Several problems were encountered in the development of the hybrid fabrication process for Plate C. First was the adhesion of the SU-8 to the nickel substrate throughout the process. This adhesion problem was solved by adding the sandblasting step to the substrate preparation phase. The roughened surface provides a strong enough mechanical bond for the SU-8 to adhere throughout the microfabrication process. The second problem was with the drilled holes in the substrate for the fasteners and supply conduits. When left unfilled, spin coating of the resist resulted in a nonuniform layer of SU-8, with the thickness going to zero near the holes. Several alternatives were considered for temporarily filling the holes during microfabrication. The material had to provide a level fill of the holes and permit spinning a good layer of SU-8, survive the pre- and

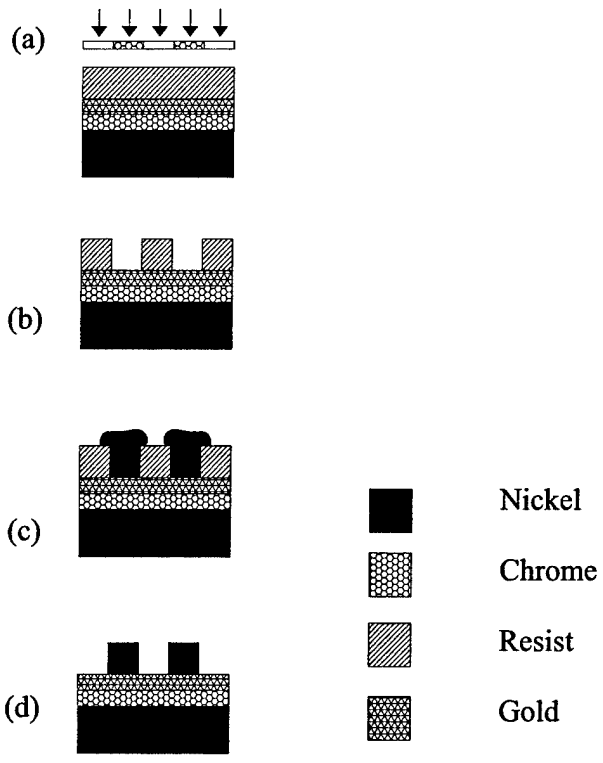

Figure 36. Microfabrication steps in forming nickel microstructures on a nickel 201 substrate.

post-baking of the UV resist, and yet be easily removable at the end of the process. After considerable experimentation, PMMA was found to be the material best suited to the temporary filling of the holes. Finally, lapping of both sides of the plate to a uniform height was found to be a highly variable process. Careful control of all parameters was necessary to obtain a good result. The need for a lapping/polishing process on each side of the plate exacerbated the problem.

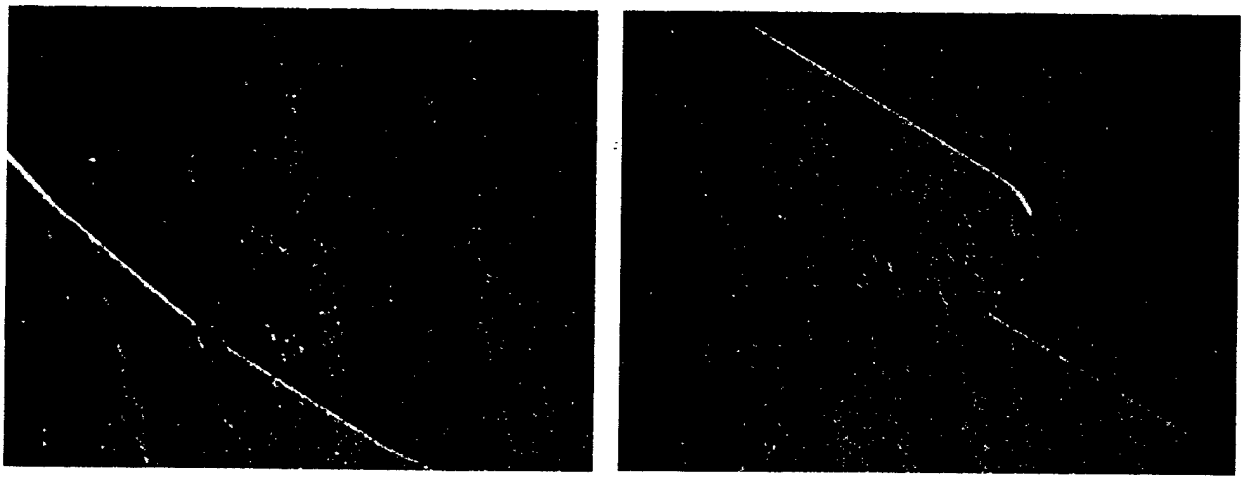

Figure 37. Optical photograph of air microchannels (left) and air swirl chamber (right) consisting of SU-8 on gold substrate. The fluid passages are 90 μm higher than the exposed substrate.

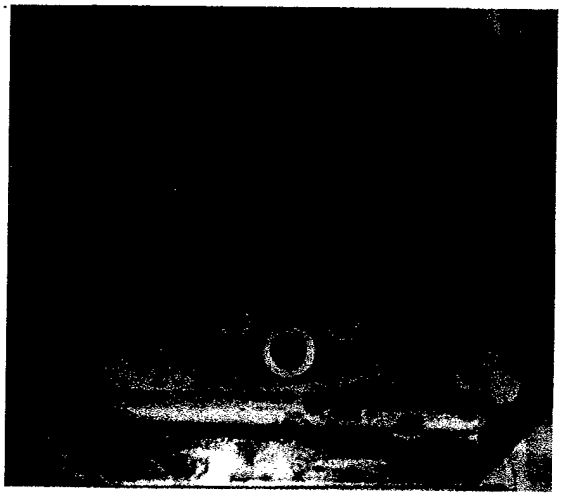

Figure 38. Optical photograph of the fuel side of Plate C immediately after completion of electroplating, with resist intact. The lighter areas are electroplated nickel and the darker areas the remaining SU-8.

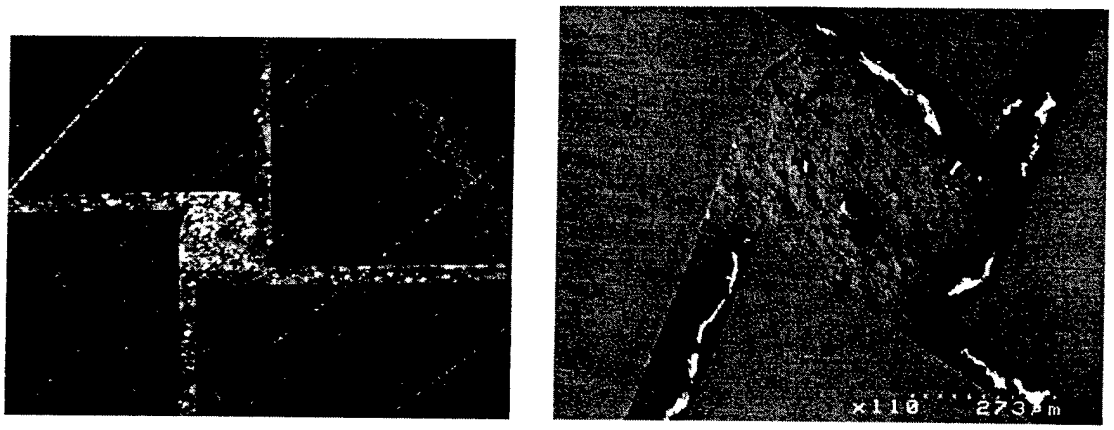

Figure 39. Views of air side swirler and micro-nozzle exit (~110 μm diameter) on Plate C. (a) Optical photograph of an electroplated air swirler and (b) SEM photograph of swirler and micro-nozzle. The light material is resist residue. The rough substrate surface is due to the sandblasting of the nickel substrate to enhance resist adhesion.

Fabrication – Ceramic Fuel Injectors

LSU currently completing program with CoorsTek (Golden, CO) to develop techniques for injection molding ceramic micro-components using LIGA-fabricated mold inserts. Work to date has been with CoorsTek standard bodies for alumina and YTZP (Figure 40). Results have shown that the critical parameter for good mold penetration is to start with nanoscale ceramic particles in the body. Methods for assembling metal-ceramic composites have been demonstrated. Alumina parts are partially sintered and placed in proximity to each other. Molten metal is drawn by capillary action into the intervening space and the ceramic pores, forming a metal-ceramic composite part. The resulting micro-channels are not obstructed by the metal. This may represent a path to fabricating a higher temperature-capable thermo-mechanical actuator in the future. In addition, LSU has purchased a Battenfeld 500/200 CDK-SE injection molding machine to support further development of ceramic molding work.

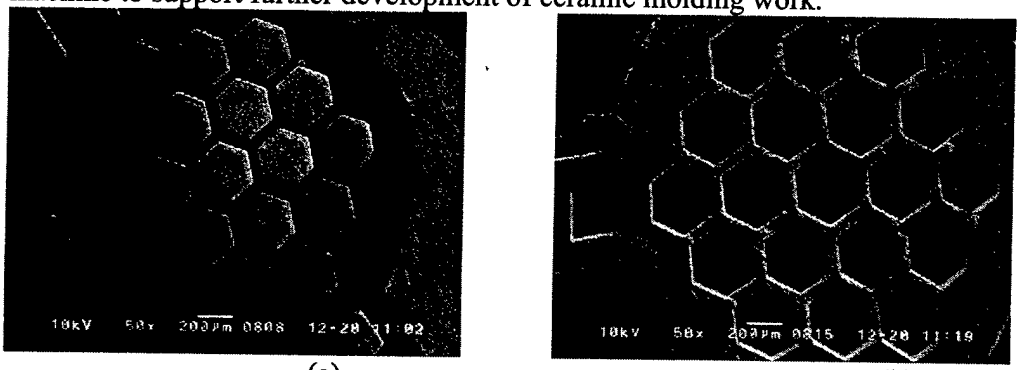

(a) (b)

Figure 40. Injection molded ceramic microstructures from standard CoorsTek bodies: (1) YTZP; (2) 99.8% alumina.

Mold inserts for injection molding ceramic fuel injector components were produced with the LIGA process at LSU (Palaparti, et al., 2003). Mold inserts were one-inch diameter plugs with the LIGA structures on the top face. These were sent to CoorsTek (Golden, CO) and both alumina and YZTP were injection molded into the parts. Some parts were sintered as individual components (Figure 41(a)), but a set of ten in each material were separated out for processing in the partially-debinded state. Excess material was milled off the back of the structures until the remaining piece was 1.5 mm thick; removal additional material produced samples too fragile to handle. Nozzles were laser drilled through the thinned parts (Figure 41(b)). Exit holes were on the order of 100 μm and entrance holes 2.5-3 times larger. The YZTP was more easily drilled. Sintering, currently underway, will reduce the hole diameters.

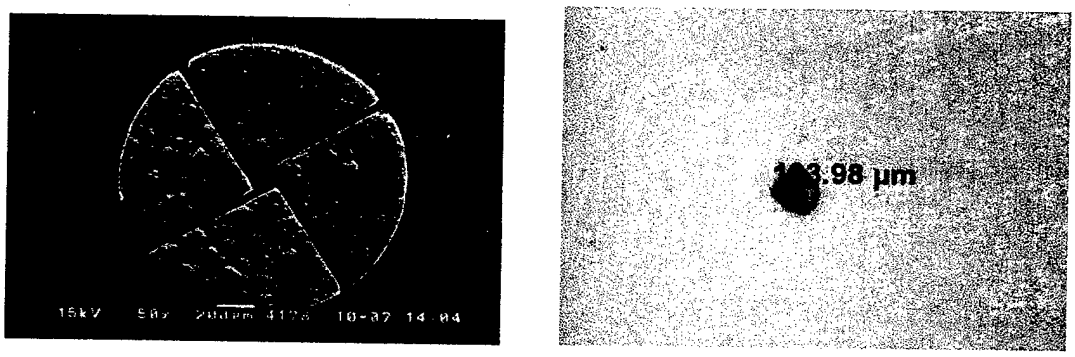

Figure 41. Injection molded ceramic fuel injector components. Mold inserts were fabricated using the LIGA process at LSU and injection molded at CoorsTek (Golden, CO). (a) Air swirler in YZTP. Good definition of the primary structure; (b) Injection nozzles were laser-drilled in some partially-debinded ceramic parts. Close-up of laser exit hole at 104 μm diameter on a partially-debinded piece.

Fabrication – Multi-layer Microfabrication

An alternative to the hybrid process for manufacturing an array of micro fuel injectors described above would be to make the parts in a multi-layer microfabrication process. Each layer would be patterned lithographically, electroplated, lapped, and then the next layer would be added on following the same sequence. Materials would be restricted to high-temperature metals that could be electrodeposited (Namburi, 2001). One of the critical steps would be lithographically patterning a post for the micro-nozzle and electrodepositing a metal plate around it. This step would produce a free-standing post of photoresist, which would have to adhere to the substrate and survive handling during electroplating. A UV lithography mask with different diameter free-standing posts was designed and purchased. Initial test exposures using SU-8 showed that the resist post could survive the lithography processing. Additional work would be required to form tapered posts suitable for micro-nozzles.

VI. ACTUATOR

Objectives

The goal for this aspect of the project was to design a microfabricated valve that could be distributed in large numbers over the walls of a smart combustor and adjust local air flow in response to non–uniform combustion. The first step toward this goal was to design a thermo-mechanical valve that would open and close as the temperature changed. The tasks undertaken were:

- Parametric design of the valve;
- Development of the required fabrication processes;
- Fabrication of prototype valves for test and evaluation;

Parametric evaluation of design parameters was based on the development of quasi-static analytical, finite element (FE), and dynamic models of the proposed valve. The models were used to evaluate how different configuration changes would affect the predicted performance of the valves (Datta, 2001a, 2001b, 2003). Two processes were needed to fabricate the prototype valves, a two- mask aligned exposure process to deposit high and low coefficient of thermal expansion (CTE) materials in the same layer and the controlled electrodeposition of an Invar-like (low CTE) alloy in deep, high aspect ratio recesses. The first two tasks were successfully completed, and prototype devices are being fabricated.

Valve Design

Basic Structure and Mechanism: The actuation mechanism selected was a direct thermo-mechanical conversion of the temperature input into a deflection through differential coefficients of thermal expansion in a bimorph structure. Thermo-mechanical deflection is a well-known principle and calculations of the deflection of a microscale cantilever bimorph were presented by Chu et al. (1993). A simple cantilever actuator structure has two drawbacks. First, the deflections possible with the range of suitable materials were insufficient unless a very long beam was used. Second, the cantilever tip is at an angle to the base of the beam, making the concatenation of multiple, shorter cantilever beams to form a compound actuator difficult.

In order to address those problems, the valve design incorporated the thermo-mechanical bimorph into the 'recurve' actuator configuration of Ervin and Brei (1998) for piezoelectric polymers, as shown in Figure 42. While the deflection at the midpoint of the recurve element is less than for a simple cantilever of the same length, the combination of two bimorphs opposing each other produces a parallel displacement of the endpoint relative to the base. Recurve elements can be combined into arrays to obtain greater net deflections or forces. By reversing the positions of the high and low coefficient of thermal expansion materials, pull-type actuators can be fabricated. One possible configuration of the valve would combine a push-and-pull actuator, as shown in the schematic of Figure 43.

The arrangement of the high CTE and low CTE sections of the recurve schematic shown in Figure 42 is not acceptable for microfabrication, since the elements of the different materials have only point contact. For use in a workable device, the modified configuration shown in Figure 44 was adopted. Each of the segments is in surface contact in the new arrangement, providing better strength, better mechanical contact, and a better electrode for electrodeposition.

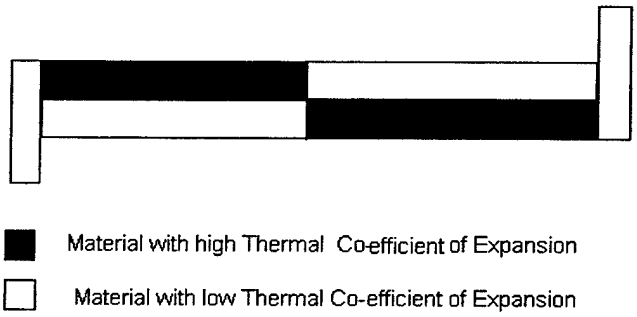

Figure 42. Schematic of a recurve thermo-mechanical actuation element based on bimorphs with each section having a different coefficient of thermal expansion.

Performance Calculations: Analytical calculations were performed to predict the steady-state response of a 25-element thermo-mechanical recurve actuator with 500 μm-tall structures. The high-CTE material was assumed to be nickel, and the low-CTE material was assumed to be an Invar-like NiFe alloy (36% Ni, 64% Fe). The deflections are for a 200 C temperature change. Figure 45(a) shows the variation in endpoint deflection and force as the length and thickness of the bimorph layers are changed. Increasing the bimorph layer thickness raises the endpoint force but decreases the deflection. Increasing the length of the bimorph elements increases the overall deflection, with a corresponding reduction in the endpoint force. Finite element simulations were compared to the results of the analytical model. A thermo-mechanical bond graph model was used to predict the dynamic response of the actuator.

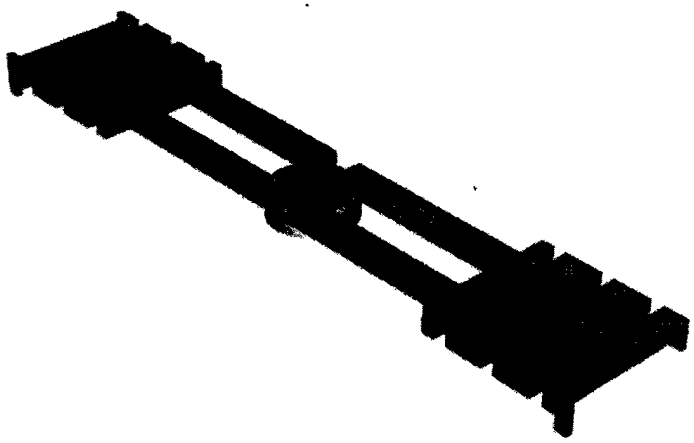

Figure 43. Schematic of thermal recurve actuators arranged in a push-pull configuration with the valve cover in the center.

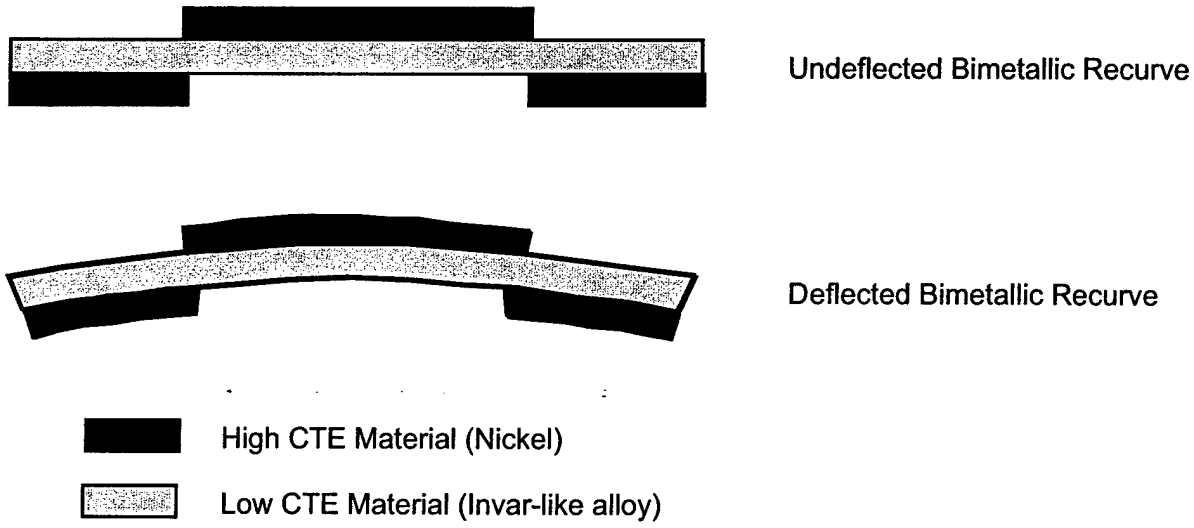

Figure 44. Schematic of bimetallic recurve element showing the relative positions of the two different metals in the prototype microfabricated recurve element and the deflection that occurs when the temperature increases.

Fabrication

Material Selection and Electrodeposition: During the first year of the project the two bimorph elements were expected to be nickel (CTE of 13.1 μm/m °C @ 20 °C) and chrome (6.2 μm/m °C) based on high temperature properties and the difference in coefficients of thermal expansion (CTE). These would not be suitable in the gas turbine environment, but would provide a proof of concept of the valve function. Electrodeposition of chrome into high-aspect-ratio micro-cavities was not successful, so an alternative material was selected for the low CTE material in the bimorph.

Bulk Invar (64% Fe, 36% Ni) has a CTE ranging from 1.3 μm/m °C @ 20 °C to 4.18 μm/m °C @ 250 °C, so electrodeposition of these alloys was the focus of the prototype development effort. Reports in the literature (Phan, et al., 1991; Phan, et al., 1994) showed that Invar-like NiFe alloys could be electrodeposited in thin films. While the methodology for electrodepositing nickel into deep recesses was well-established, a process for deposition of high-aspect-ratio structures using an iron-rich nickel-iron alloy had not been demonstrated. A pulse plating process was applied to electrodeposition of an Invar-like alloy into deep microstructures (Namburi, 2001; Datta, 2001b). A Hull cell study was carried out to find the range of current densities that would produce good quality electroplated NiFe alloys with the desired composition. Once a range of suitable current densities was identified, deposits were made into an array of LIGA micro-patterned cavities up to 300 μm deep. Electrodeposition into deep recesses is diffusion-driven. Pulse plating was used to accommodate diffusion and to reduce the side reactions, which were primarily hydrogen forming. It was found that short on-times and long off–times were necessary to obtain uniform composition along the length of a post. A field of 300 μm tall, 120 μm X 120 μm micro-posts is shown in Figure 46. The composition of a representative micro-post was evaluated using WDS analysis (Figure 47). After adjusting the duty cycle to obtain uniform composition, it was found that the iron concentration in the sample was a direct function of the molar concentration of ferrous sulfate in the plating bath. A patent has been filed covering the electrodeposition process.

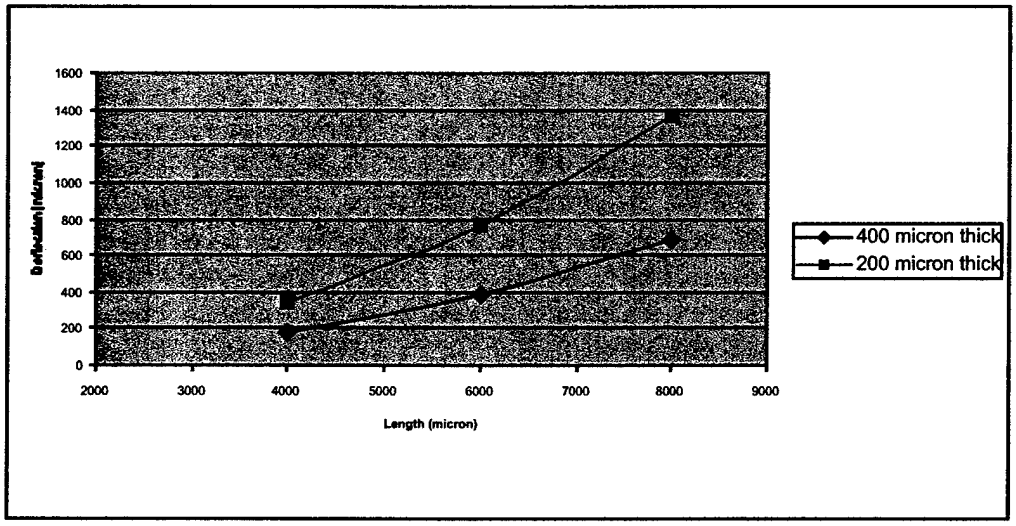

(a)

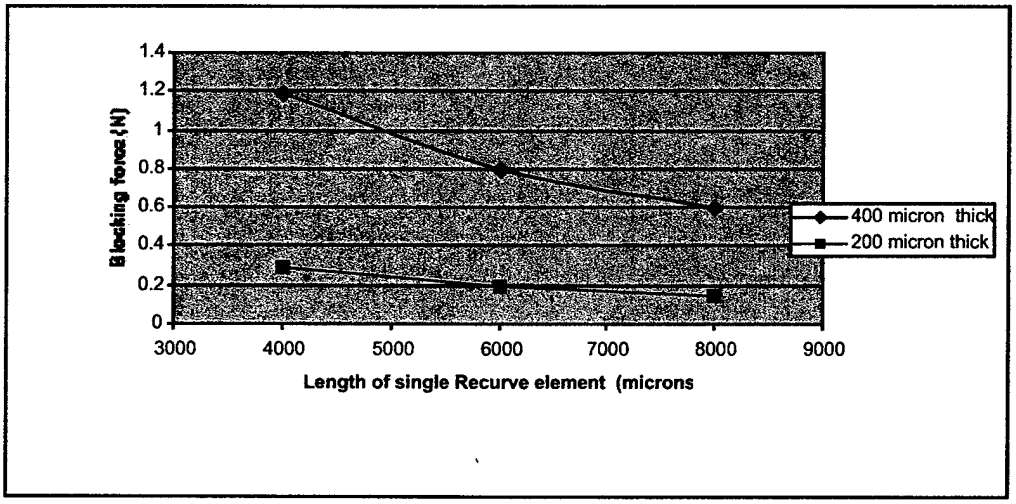

(b)

Figure 45. Variation in the deflection (a) and endpoint force (b) for an actuator comprised of 25 recurve elements. The structures are 500 μm tall with the bimorph materials being Ni and Invar-like NiFe. The temperature change is assumed to be 200 C. Deflection and force are shown as functions of the length of the recurve element, ranging from 4 mm to 8 mm, for two total bimorph widths, 200 μm and 400 μm. There is a trade-off between the increased deflection obtained with longer elements and the corresponding decrease in the deflection.

Figure 46. SEM photographs of electroplated Invar-like NiFe alloy posts. Top view of 120 μm X 120 μm X 300 μm posts.

All of the performance estimates have assumed that the CTE of the bulk material holds for the electrodeposited materials. This is probably a good assumption for the nickel. Initial results show that the electrodeposited NiFe alloy has a low coefficient of thermal expansion (CTE) and that it decreases after annealing. CTE tests were carried out at Stork Technimet (New Berlin, WI). Only a few samples have been plated, annealed, and tested, so the annealing process is not completely understood. In a patent (Sokolowski, et al., 1995) for bulk Invar formed from powdered metal, a fairly complex annealing sequence is outlined to obtain the low CTE and dimensional stability. The electrodeposit does not require consolidation like the powdered metal, so a simpler process may be possible.

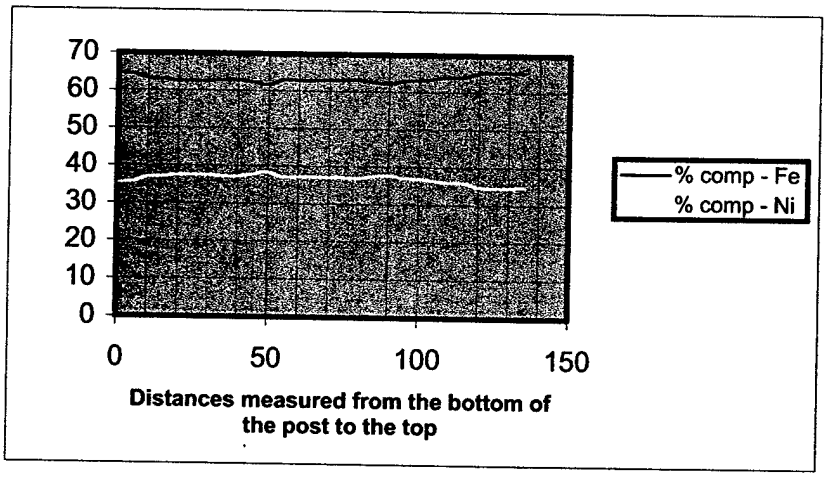

Figure 47. Variation in the composition of the Invar-like alloy along the length of a 135 μm post. Variation is less than 1% along the length. Larger variation at the ends is due to plating base residue.

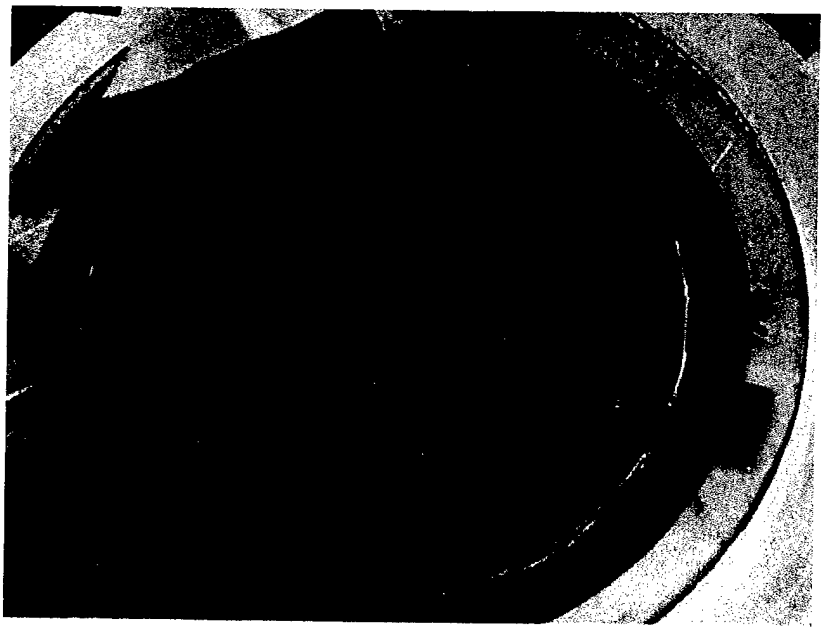

Figure 48. X-ray mask for test devices.

Fabrication Process: A mask set for test recurve devices for test and evaluation was made. One of the X-ray masks is shown in Figure 48. There are twelve different actuator designs on the mask set with bimorph lengths of 8 mm, 12 mm, and 16 mm and bimorph widths of 200 μm and 400 μm. Both push and pull configurations of each design were included. The X-ray masks were produced using a technique developed at LSU for transferring an optical lithography mask pattern to a graphite membrane (Desta, et al., 2000). A schematic of the process for producing the test structures is shown in Figure 49. Three layers are necessary. In the first layer, which may use either optical or X-ray lithography, a base layer is formed on the substrate (Figure 49(a)). The base layer includes a nickel pedestal for the bimetallic recurve cantilever and a sacrificial layer, probably titanium (Ti), beneath the suspended cantilever portion of the structure. The second layer will add the nickel portion of the bimorph structure (Figures 49(b) and 49(c)) and the third layer will electrodeposit the alloy segments of the bimetallic recurve. The second and third layers each consist of an X-ray lithography step, electrodeposition into the pattern, and lapping/polishing back to the desired height. The final step is the removal of the remaining X-ray resist and the sacrificial layer to release the devices. This is followed by annealing of the alloy and testing of the devices.

Final Product: Test structures, ranging from single recurve elements to ten element stacks, were successfully fabricated and released from the substrates for testing. Electroplated structures still embedded in the resist after lapping are shown in Figure 50(a). The bright/lighter surface is the nickel and the gold surface is the nickel-iron alloy. Sample free-standing released structures are shown in Figure 50(b).

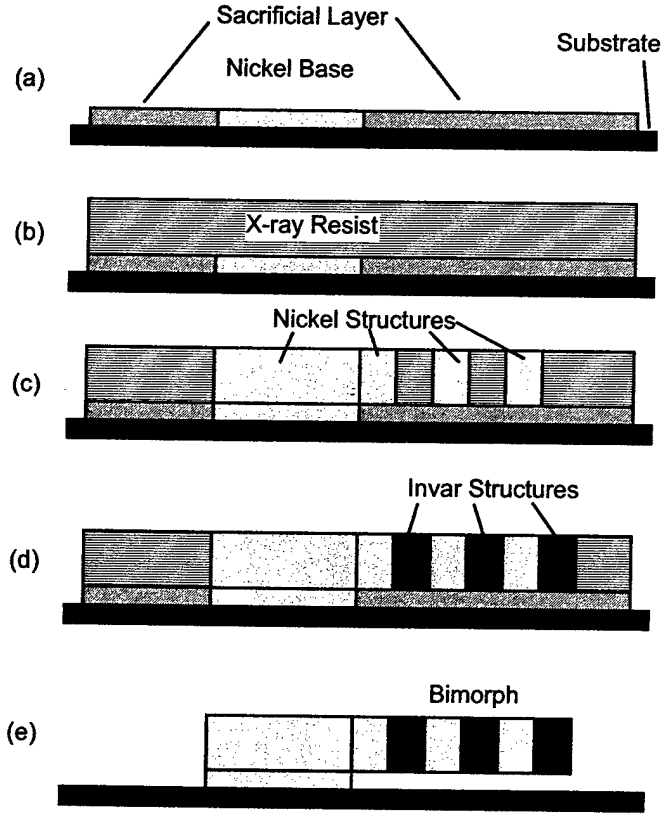

Figure 49. Schematic of test structure fabrication process: (a) First layer containing nickel base plate and sacrificial layer beneath cantilever; (b) Thick X-ray resist layer added over lapped/polished base layer; (c) Nickel portion of bimetallic recurves deposited into resist pattern; (d) Alloy portion electrodeposited into lithographically defined pattern; and (e) Resist and sacrificial layer removed leaving testable structures.

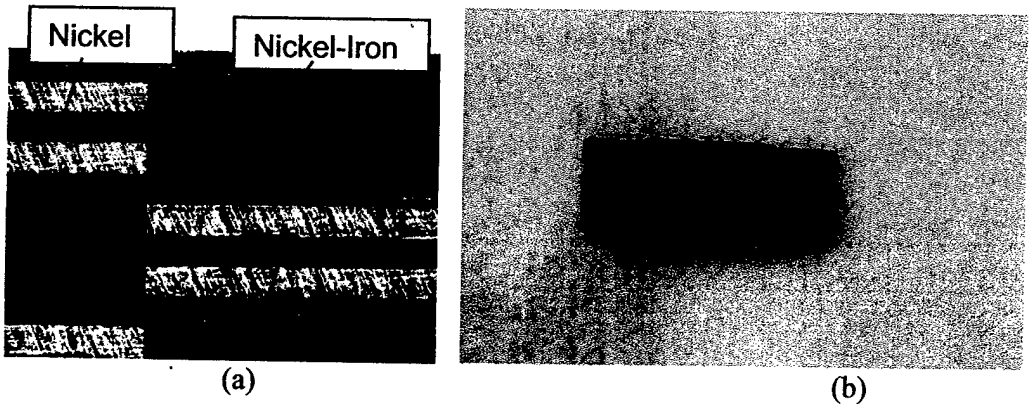

Figure 50. Fabricated bimorphs. Test structures ranging from single bimorphs to ten element stacks were successfully fabricated and released from the substrate for testing.

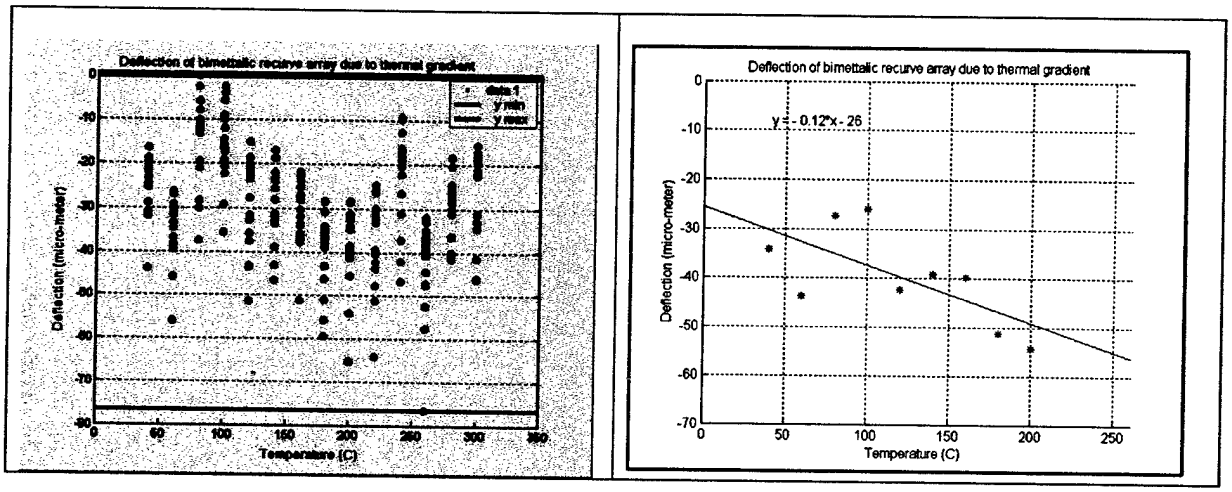

Figure 51. Representative test data for the bimorphs. Devices were tested in 3-point bending in a Dynamic Materials Analyzer (DMA, Q-800) up to 300 °C. Raw data trace for a single recurve element. The temperature was stepped in 20 °C increments and held for one minute at each temperature to all equilibration. The initial deflection at temperature is the top data point and the deflection at one minute is the bottom data point. Figure on the right is a linear fit to the steady state temperatures in the figure on the left.

Performance Evaluation

Test Equipment: All measurements were made using a TA Instruments (New Castle, DE) Q-800 Dynamic Mechanical Analyzer (DMA) at CAMD. The DMA includes several different clamps including a 3-point bending clamp, a force rebalance transducer, air bearings, and a direct drive motor to enable accurate measurements of deflection and force over a temperature range of -150 °C-600 °C. For the tests of the bimorphs the 3-point bending clamp was used and the temperatures were stepped in 20 °C increments from 35 °C to 300 °C. At each temperature point deflection was recorded over one minute as the device reached equilibrium, then the temperature was again increased.

Results: Data for a 2-element recurve device are shown in Figure 51. The raw data in Figure 51 includes all of the measurements recorded over one minute at each temperature. The bottom data point was the deflection at one minute. The initial deflections measured at 40 °C and 60 °C are believed to be anomalous due to adjustment of the clamp, and are being checked by repeat measurements. For temperatures from 80 °C to 220 °C the relationship between the temperature and deflection is essentially linear (see figure on right). Above 240 °C the actuator reverses its deflection as temperature increases. This is expected since the low-CTE property of Invar is a magnetic effect and the Curie temperature for Invar is about 230 °C (Marsh, 1938). When the temperature of the Invar increases past the Curie temperature, the thermal expansion properties return to those of a normal alloy.

VII. REFERENCES

Bardina, J, Ferziger, J.H. and Reynolds, W.C., 1983, Improved turbulence models based on large eddy simulations of homogeneous, incompressible turbulent flows, Report TF-19, Thermosciences Div., Dept. Mech. Eng., Stanford Univ.

Baurle, R.A., and Gruber, M.R., 1998, A Study of recessed cavity flowfields for supersonic combustion applications, AIAA 98-0938.

Ben-Yakar, A., and Gany A., 1994, Experimental study of a solid fuel scramjet, AIAA Paper 94-2815, 30th AIAA Joint Propulsion Conference, Indianapolis, IN, June 27-29, 1994.

Ben-Yakar A., Kamel, M.R., Morris, C.I., and Hanson, R.K., 1998, Hypersonic combustion and mixing studies using simultaneous OH-PLIF and schlieren imaging, AIAA Paper, 98-0940, 36th AIAA Aerospace Sciences Meeting and Exhibit, Reno, NV, January, 12-15, 1998.

Chakka, P., Mancilla, P., Acharya, S., 1999, Flame stability in a trapped vortex spray combustor, Presented at APS Conference, New Orleans, 1999.

Chu, W.-H., Mehragany, M., and Mullen, R. L., 1993, Analysis of tip deflection and force of a bimetallic cantilever microactuator, Journal of Micromechanics and Microengineering, 3, 4-7.

Datta, P., 2001a, *Design and Fabrication of a Thermomechanical Micro-Actuator*, M.S. Thesis, Department of Mechanical Engineering, Louisiana State University.

Datta, P., Namburi, L., Podlaha, E.J., Acharya, S., and Murphy, M.C., 2001b, Design and fabrication of a thermomechanical micro-actuator for high temperature applications, presented at *Workshop on High Aspect Ratio Microsystems Technology (HARMST 2001), Baden-Baden, June 17-29, 2001.*

Datta, P., Sathe, M., Namburi, L., Podlaha, E.J., Acharya, S. and Murphy, M.C., 2003, "Microfabricated bimetallic actuator," in *MEMS Components and Applications for Industry, Automobiles, Aerospace, and Communication II,* ed. S.W. Janson, Society of Photo-optical Instrumentation Engineers (SPIE), Volume 4981, pp. 83-94.

Desta, Y., Aigeldinger, G., Zanca, K.J., Coane, P. , Göttert, J., and Murphy, M.C., 2000, Fabrication of graphite masks for deep and ultra-deep X-ray lithography, in Materials and Device Characterization in Micromachining III, eds. Y. Vladimirsky and P. Coane, SPIE, Bellingham, WA, vol. 4175.

Ervin, J.D. and Brei, D., 1998, Recurve piezoelectric-strain-amplifying actuator architecture, IEEE/ASME Transactions on Mechatronics, 3(4), 293-301.

Hsu, K.-Y., Goss, L.P., and Roquemore, W.M., 1998, Characteristics of a trapped-vortex combustor, J. of Propulsion and Power, Vol. 14, No. 1, pp. 55-65

Jorgenson, D., 1999, Personal communication with EDM machinist at Optimation, Inc., Burr-Free Machining Division, Midvale, UT.

Katta, V.R. and Roquemore, W.M., 1996, Numerical studies on trapped-vortex combustor, AIAA 96-2660.

Katta, V., and Roquemore, W.M., 1998, Study on trapped-vortex combustor-Effect of injection on flow dynamics, J. of Propulsion and Power, Vol. 14, No. 3, pp. 273-281.

Ling, Z., Lian, K. and Jian, L., 2000, Improved patterning quality of SU-8 microstructures by optimizing the exposure parameters, in Advances in Resist Technology and Processing XVII, ed. F.M. Houlihan, SPIE, Bellingham, WA, vol. 3999.

Little, Jr., B.H., and Whipkey, R.R., 1979, Locked vortex afterbodies, J. of Aircraft, Vol. 16, No. 5, pp. 296-302.

Mair, W.A., 1965, The effect of a rear-mounted disc on the drag of a blunt-based body of revolution, The Aeronautical Quarterly, Vol. 10, Pt. 4, Nov. 1965, pp. 350-360.

Marsh, J.S., 1938, *The Alloys of Iron and Nickel*, McGraw-Hill, Inc., New York, NY, p.45.

Mathur, T., Streby, G., Gruber, M., Jackson, K., Donbar, J., Donaldson, W., Jackson, T., Smith, C., and Billig, F., 1999, Supersonic combustion experiments with a cavity-based fuel injector, AIAA Paper 99-2102.

Namburi, L., 2001, *Electrodeposition of NiW Alloys into Deep Recesses*, M.S. Thesis, Department of Chemical Engineering, Louisiana State University.

Palaparti, D., Landin, S., Simmons, H., Ritland, M., Sommerfeldt, R., Desta, Y.M., Morris, T.E., and Murphy, M.C., 2003, "Injection molded ceramic micro-components," presented at *HARMST 2003, Monterey, CA, June 15–17,2003.*

Phan, N.H., Schwartz, M. and Nobe, K. ,1991, Electrodeposition of Fe-Ni-Co alloys, Part 1: Direct current deposition, Journal of Applied Electrochemistry, 21:672-677.

Phan, N.H., Schwartz, M. and Nobe, K., 1994, Pulsed electrodeposition of Fe-Ni-Co alloys, Electrochemical Acta, 39(3):449-453.

Roudakov, A.S., Schikhmann Y., Semenov V., Novelli Ph., and Fourt O., 1993, Flight Testing an Axisymmetric Scramjet – Russian Recent Advances, IAF Paper 93-S.4.485, 44th IAF Congress, Graz, Austria, Oct. 1993.

Roquemore, W. M., 2003, A Historical perspective of the trapped vortex combustor, 3rd Joint Meeting of the U. S Sections of the Combustion Institute, Chicago, March 16-19 2003

Segal, C., Owens M.G., Tehranian, S., and Vinogradov V., 1997, Flameholding configurations for kerosene combustion in a Mach 1.8 airflow, AIAA Paper, 97-2888, 33rd Joint Propulsion Conference and Exhibit.

Sokolowski, W.M., Lane, M.S., Hsieh, C.H., and O'Donnell, T.P., 1995, *Ultrahigh-Purity Dimensionally Stable Invar 36*, US Patent 5,476,633, December 19, 1995.

Speziale, C.G., 1985, Galilean Invariance of subgrid scale stress models in large eddy simulation of turbulence, J. Fluid Mech. Vol. 156, pp. 55-62.

Sturgess, G., and Hsu, K.-Y., 1997, Entrainment of main-stream Flow in a trapped-vortex combustor, AIAA-97-0261, 1997.

Tishkoff, J.M., Drummond, J.P., Edwards, T., and Nejad, A.S., 1997, Future direction of supersonic combustion Research: Air Force/NASA Workshop on Supersonic Combustion, AIAA Paper 97-1017.

Tyagi, M., and Acharya, S., 2001, Large Eddy Simulations of complex turbulent flows using Immersed Boundary Methods, Third AFOSR International Conference on Direct Numerical Simulation and Large Eddy Simulation, Arlington, August 2001

Tyagi, M., and Acharya, S., 2003, Larged Eddy Simulations in complex geometries using the Immersed Boundary Technique, ASME International Mechanical Engineering Congress and Expo, Wasshington D.C., Nov. 2003

Yusof, J. Mohd., 1996, Interaction of massive particles with turbulence, Ph.D. Dissertation, Cornell University

Zang, Y., Street, R.L. and Koseff, J.R.. 1993, A dynamic mixed subgrid scale model and its application to turbulent recirculating flows, Phys. Fluids A Vol. 5 no. 12 pp. 3186-3196